nature communications

Article

https://doi.org/10.1038/s41467-025-59331-y

N^6-methyladenosine modifications stabilize phosphate starvation response–related mRNAs in plant adaptation to nutrient-deficient stress

Received: 25 April 2024

Accepted: 16 April 2025

Published online: 01 May 2025

Check for updates

A list of authors and their affiliations appears at the end of the paper

N^6-methyladenosine (m^6A), an abundant internal mRNA modification, is induced by various stress conditions and post-transcriptionally regulates gene expression. However, how m^6A modifications help plants respond to nutrient-deficiency stress remains unclear. Here, we profile high-confidence m^6A modifications in Arabidopsis transcriptome-wide under normal and inorganic orthophosphate (Pi)–deficient conditions (−P). High-confidence m^6A modifications are identified using synthetic modification-free RNA libraries for systematic calibration. Pi starvation induces widespread m^6A modifications, mediated by the Pi starvation response (PSR) master regulator PHOSPHATE STARVATION RESPONSE1 (PHR1) and its family members. Many Pi starvation–induced (PSI) m^6A modifications occur on PSR-related mRNAs, including *PHR1*. In addition, PHR1 proteins interact with the m^6A writers MRNA ADENOSINE METHYLASE (MTA) and METHYLTRANSFERASE B (MTB) in nuclei under −P conditions. m^6A modifications facilitate systemic PSR signaling, as reflected by the reduced Pi content and PSR signaling in a knockdown artificial miRNA line targeting *MTA*, which shows a global decrease in m^6A. Transcriptome-wide mRNA decay analysis reveals that PSI-m^6A increases the stability of PSR-related mRNAs, but not through alternative polyadenylation site shifts. Analysis of transgenic plants with mutations in m^6A loci demonstrates that m^6A stabilizes *PHR1* transcripts via a positive feedback loop. Our findings indicate that PSI-m^6A modifications facilitate PSR signaling by enhancing the stability of certain mRNAs, shedding light on the role of m^6A modifications in nutrient stress responses in plants.

The most prevalent internal covalent modification of eukaryotic messenger RNAs (mRNAs) is the methylation of adenines to produce N^6-methyladenosine (m^6A), which occurs predominantly near the 3′ ends[1–3]. The m^6A modification is reversibly added and removed by evolutionarily conserved methyltransferases (writers) and demethylases (erasers), respectively[4–8]. In Arabidopsis (*Arabidopsis thaliana*), the methylation reaction is primarily catalyzed by a multi-protein complex comprising MRNA ADENOSINE METHYLASE (MTA; ortholog of human METTL3), METHYLTRANSFERASE B (MTB; ortholog of human METTL14), FKBP12 INTERACTING PROTEIN37 (FIP37; ortholog of human WTAP), VIRILIZER (VIR), and HAKAI[9–13]. In a small subset of mRNAs, m^6A modifications are also produced by another

e-mail: wangzhiye1@zju.edu.cn

methyltransferase, FIONA1 (FIO1; ortholog of human METTL16)[14–16]. The m^{6}A methyl groups can be removed by the demethylases ALKBH9B and ALKBH10B (orthologs of human ALKBH5)[17–19].

The underlying mechanisms and biological functions of m^{6}A have been studied by profiling this modification across the transcriptomes of plants at various developmental stages and under different growth conditions[2,3]. Transcriptome-wide m^{6}A mapping usually involves immunoprecipitation of methyl-RNA combined with high-throughput RNA sequencing (MeRIP-seq or m^{6}A-seq); however, the fidelity of this method is compromised by the non-specific binding of the anti-m^{6}A antibody[20–22]. To improve the reliability of m^{6}A-seq, Luo and colleagues developed a method for the systematic calibration of epitranscriptomic maps using synthetic modification-free RNA library controls that resembled the endogenous transcriptome in terms of sequence and expression diversity[22]. This synthetic RNA library approach serves as a more robust and rigorous control[22] than previously employed calibration controls, such as methyltransferase gene knockout and in vitro demodification. Although this gold-standard negative control has been used in epitranscriptome mapping studies of animals and viruses[23,24], it has not previously been used for plants.

Environmental stress dynamically alters the m^{6}A landscape[3,24,25], reflecting the important regulatory functions of this modification in the adaptation to stress. In plants, the dynamic of m^{6}A modifications responds to several abiotic and biotic stresses, such as salt[26,27], drought[28,29], heat[30], cold[31], excess light[32], viral pathogens[33,34], and fungal diseases[35]. However, the underlying functions of m^{6}A in stress adaptation are not well understood. Several studies have demonstrated that stress causes dynamic m^{6}A deposition on specific stress-responsive transcripts, which mainly affects their stability. For example, salt stress–induced m^{6}A not only stabilizes transcripts involved in the salt-stress response[27], but also destabilizes transcripts involved in the negative regulation of this response[26]. These contrasting effects on RNA stability were also observed in the m^{6}A-mediated regulation of development[10,17,36–38], pointing to a complex relationship between m^{6}A modification and RNA decay. Despite these insights, a transcriptome-wide RNA half-life assay with m^{6}A profiling under normal and stress conditions has not yet been performed in plants.

Nutrient deficiency is a major limiting factor in global crop production[39,40]; however, the regulation of m^{6}A modification in the plant response to nutrition-deficiency stresses remains unclear. Phosphorus (P) is essential for all life on Earth[41–43]. P is a key element for photosynthesis, an important component of macromolecules such as nucleic acids, and is involved in posttranslational modifications and the biosynthesis of essential metabolites[44]. Plants take up P as orthophosphate (Pi) from the soil. Studies of the plant response to Pi starvation are ecologically and agriculturally important because soils in many parts of the world have low levels of available Pi due to its immobility, low solubility, or the general lack of this mineral[45,46].

To withstand environmental Pi limitation, plants have evolved a complex Pi-starvation response (PSR) comprising a series of developmental and physiological changes[47,48]. The evolutionarily conserved PHOSPHATE STARVATION RESPONSE1 (PHR1) and the related PHR1-like (PHL) family, collectively termed PHRs, act as central transcriptional regulators of systemic PSR signaling[49–52]. PHRs belong to the GARP transcription factor (TF) family and possess a MYB-like DNA-binding domain and a coiled-coil domain[49,50]. Upon Pi-deficiency, PHR1 forms homodimers or heterodimers with PHL1 and directly binds to a pseudo-palindromic DNA sequence (GNATANC; P1BS) in the promoters of many Pi starvation–induced (PSI) genes to upregulate their expression[49,53]. Transcriptome analysis revealed that PHRs also indirectly regulate the expression of some Pi starvation–decreased (PSD) genes[53], although the underlying mechanism remains elusive. Besides transcriptional reprogramming, PHRs regulate changes in chromatin accessibility[54], lipid remodeling[55], metabolic changes[56], and mycorrhizal symbiosis[57] in response to Pi starvation. However, it is not known whether PHRs also regulate m^{6}A modification and thereby RNA stability under Pi starvation. As PHRs are fundamental regulators of the PSR, their activity is extensively regulated. PHR1 activity is inhibited through physical interactions with SPX (named after yeast Syg1 and Pho81 and mammalian XPR1) proteins in response to Pi status[42,58–61]. Other types of post-translational regulation of PHR activity were also reported, including protein degradation[62], sumoylation[63], and phosphorylation[64]. However, the regulation in *PHR1* transcript levels remains uncharacterized.

Here, we performed m^{6}A-seq with systematic calibration using synthetic modification-free RNA libraries and produced high-confidence m^{6}A profiles in Arabidopsis under normal and Pi-deficient stress conditions. We determined that Pi starvation induces global m^{6}A modifications, largely mediated by PHR proteins. Many PSI-m^{6}A modifications are deposited in PSR-related transcripts, including *PHR1* mRNA. Although PHRs do not regulate PSI-m^{6}A modifications through direct transcriptional regulation, PHR1 interacts with the m^{6}A writers MTA and MTB in nuclei under −P conditions. A genome-wide RNA decay assay demonstrated that PHR-mediated PSI-m^{6}A modifications stabilize PSR-related mRNAs. PAS-seq 2 data indicated that PSI-m^{6}A did not impact RNA stability via alternative polyadenylation site (APA) shifts. Furthermore, mutations in putative m^{6}A-loci in the 3′ untranslated region (UTR) of *PHR1* mRNA led to shortened RNA half-lives and partial *phr1* complementation, confirming that m^{6}A stabilizes *PHR1* transcripts as a positive feedback mechanism to promote PSI signaling and stress adaptation upon Pi starvation.

Results

Transcriptome-wide profiling of high-confidence m^{6}A modifications using systematic calibration with a synthetic modification-free RNA library

To explore the regulatory function of m^{6}A in Pi homeostasis and signaling, we performed m^{6}A-seq to examine the effect of Pi starvation on transcriptome-wide m^{6}A levels. To correct for non-specific binding to the anti-m^{6}A antibody during m^{6}A-seq, we used a synthetic modification-free RNA library to calibrate the epitranscriptomic maps[22] (Fig. 1a).

Following the protocol shown in Supplementary Fig. 1a[22], we replicated the entire transcriptome (all mRNAs) using T7 RNA polymerase–mediated in vitro transcription (IVT) and unmodified nucleosides (referred to as IVT RNA) (Fig. 1b). We confirmed the absence of m^{6}A modifications in the synthesized no-m^{6}A IVT RNA using liquid chromatography–mass spectrometry (LC–MS/MS) (Fig. 1c). We next performed mRNA-seq, which showed that approximately 95% of the genes represented in the endogenous total mRNA were also represented in the no-m^{6}A IVT RNA. Furthermore, the global gene expression levels in the no-m^{6}A IVT RNA library were strongly correlated with those in the endogenous transcriptome (Pearson's $r = 0.954$) (Fig. 1d). The read coverages across the transcripts were also similar between the IVT RNA and endogenous mRNA libraries (Fig. 1e). These findings indicate that we successfully generated a non-m^{6}A modified IVT RNA library that closely resembled the endogenous transcriptome in terms of sequence representation and expression.

We generated two biological replicates of the m^{6}A-seq and the corresponding mRNA-seq using endogenous mRNA and synthetic no-m^{6}A IVT RNA from seedlings grown under normal (+P) and Pi-starvation (−P) conditions. We mapped the sequencing reads (approximately 20–28 million reads per sample) to the Arabidopsis TAIR10 reference genome and used the exomePeak pipeline to call the m^{6}A peaks in the transcripts of all samples using the immunoprecipitation (IP) enrichment criteria (IP/input ≥ 2, FDR < 0.05). More than 14,000 peaks were identified in the endogenous mRNAs (Supplementary Fig. 1b). Most peaks (~90%) were represented in both biological replicates, indicating high reproducibility (Supplementary Fig. 1b). In total, 12,837 peaks and 13,379 common peaks were identified in the endogenous mRNA samples under +P and −P conditions,

respectively (Supplementary Fig. 1b and Supplementary Data 1). Strikingly, numerous m^{6}A-irrelevant peaks were identified in the corresponding synthetic no-m^{6}A IVT RNA samples, indicating the non-specific binding of the anti-m^{6}A antibodies (Supplementary Fig. 1c, Supplementary Data 1). The peaks in the endogenous mRNA libraries were mainly located around stop codons and in 3′ UTRs (Fig. 1f), which is consistent with a previously published m^{6}A peak distribution[1–3]. By contrast, the m^{6}A-irrelevant peaks in the no-m^{6}A IVT RNA libraries were mainly distributed in coding sequence (CDS) regions (Fig. 1f). Moreover, VAGGUA (V = A/C/G) and RGMRGR (R = A/G; M = A/C) motifs were identified in the m^{6}A-irrelevant peaks (Fig. 1g), which are similar to the motifs identified in the IVT RNA m^{6}A-seq library in a mammalian study[22].

Next, we systematically calibrated the transcriptome-wide m^{6}A modifications with the identified m^{6}A-irrelevant peaks to remove false-positive m^{6}A peaks from the endogenous mRNA m^{6}A-seq libraries (Fig. 1h, see Methods). Approximately 2000 and 1500 false-positive peaks were removed from the +P and −P samples, respectively, accounting for 11–16% of the total peaks (Fig. 1h). Consequently, we identified 10,757 and 11,861 high-confidence m^{6}A peaks associated with 10,420 and 11,496 genes in Col-0 (WT) seedlings under +P and −P conditions, respectively (Fig. 1h and Supplementary Data 1). We also confirmed the false-positive and high-confidence m^{6}A peaks using the Integrative Genomic Viewer (IGV), finding that false-positive m^{6}A loci exhibited similar peaks in the WT endogenous mRNA and IVT RNA IPs, whereas the high-confidence peaks were only present in the WT mRNA IPs (Fig. 1i and Supplementary Fig. 1d). Furthermore, the high-confidence m^{6}A peaks exhibited stronger enrichment around stop codon and in 3′ UTR than did the uncalibrated peaks (Fig. 1j). In addition to the plant-specific UGUA motif and common RRACH (H = A/C/U) motif, we also identified a CAGR motif in the calibrated m^{6}A peaks under both +P and −P conditions (Supplementary Fig. 1e).

Therefore, the use of systematic calibration with a synthetic modification-free RNA library allowed us to identify high-confidence m^{6}A peaks under normal and Pi-deficient conditions in WT seedlings.

Pi starvation induces global changes in m^{6}A levels

Under −P, the m^{6}A levels across the transcriptome were dramatically increased in comparison with +P conditions (Fig. 2a, b). In addition, 1651 transcripts underwent de novo m^{6}A modification in response to −P conditions, while only 575 m^{6}A-modified transcripts occurred under +P conditions (Fig. 2c). We accurately identified the m^{6}A peaks that differed between +P and −P conditions using the exomePeak algorithm, with the criteria of fold change ≥ 1.5 and FDR < 0.05, excluding m^{6}A-irrelevant peaks. Pi starvation resulted in 4418 hypermethylated m^{6}A peaks (PSI-m^{6}A) across 4364 genes compared to only 323 hypomethylated m^{6}A peaks (PSD-m^{6}A) across 316 genes (Fig. 2d, Supplementary Data 1), indicating that Pi starvation enhances the production of m^{6}A modifications across the transcriptome. Compared with other published sets of genes whose m^{6}A profiles changed in response to treatment[19], major m^{6}A-hypermethylation (71.1%) and m^{6}A-hypomethylation (98.4%) in response to Pi starvation are specific (Supplementary Fig. 2a).

These PSI-m^{6}A and PSD-m^{6}A peaks were mainly located near stop codons and in 3′ UTRs, although a few peaks were located at CDSs and 5′UTRs (Supplementary Fig. 2b, c). The plant-specific UGUA motif was enriched within both PSI-m^{6}A and PSD-m^{6}A peaks at the 3′UTR (Supplementary Fig. 2d). Notably, an unreported CAGR motif was specifically enriched within PSI-m^{6}A peaks at the 3′UTR, indicating a potential link of this motif with PSI-m^{6}A function (Supplementary Fig. 2d). We performed a Gene Ontology (GO) analysis to investigate the PSI-m^{6}A hypermethylated genes. In addition to functions in phosphorus metabolism, the PSI-m^{6}A genes are involved in RNA stability, RNA splicing and 3′-end processing, rRNA processing, tRNA modification, and histone and DNA modification pathways, which are indicative of m^{6}A-mediated regulations of RNA metabolism and transcription in response to Pi starvation (Fig. 2e). PSI-m^{6}A genes are also involved in photosynthesis, defense responses, protein transmembrane transport, and protein lipidation (Fig. 2e). By contrast, PSD-m^{6}A hypomethylated genes are involved in responses to stress, inorganic anion transport, and sulfur compound biosynthesis (Fig. 2f). These results suggest that m^{6}A RNA modifications are involved in regulating multiple processes during the PSR, from transcription to RNA metabolism and ion homeostasis.

We then focused on the PSR-related genes. Given that Pi starvation triggers the altered expression of thousands of genes[53], we assessed whether the changes in m^{6}A modification were associated with changes in the expression of PSR genes. Consistent with previous studies[53], our RNA-seq data showed that thousands of genes were upregulated (−P/+P ≥ 1.5, $P < 0.05$; PSI genes) or downregulated (+P/−P ≥ 1.5, $P < 0.05$; PSD genes) by Pi-deficiency (Supplementary Fig. 2e, Supplementary Data 2). Notably, approximately one-third of the PSI genes and more than 70% of the PSD genes contained m^{6}A modifications (Supplementary Fig. 2f). Furthermore, a joint analysis of the m^{6}A-seq and RNA-seq data revealed a large number of m^{6}A-hypermethylated PSD genes (638 PSI-m^{6}A & PSD genes, accounting for ~71% of the total m^{6}A-altered PSR genes). These results suggest that m^{6}A modification might regulate the RNA levels of PSD genes in response to Pi starvation (Fig. 2g and Supplementary Data 1).

Furthermore, the transcripts of several known Pi homeostasis and PSR-signaling genes harbored m^{6}A modifications. These genes included the central PSR-signaling gene *PHR1* and its homologs[49,53], the PSR-signaling repressor genes *SPX2* and *SPX4*[58,65], the phosphate transporter trafficking facilitator gene *PHOSPHATE TRANSPORTER TRAFFIC FACILITATOR1* (*PHF1*)[66,67], the Pi efflux transporter gene *PHO1*[68], the root tip low-phosphate sensor *LOW PHOSPHATE ROOT2* (*LPR2*)[69], the diphosphoinositol pentakisphosphate kinase genes *VIP1 HOMOLOG1* (*VIH1*) and *VIH2*[70], and the vacuolar Pi transporter genes *PHOSPHATE TRANSPORTER 5;1* (*PHT5;1*) and *PHT5;3*[71,72] (Fig. 2h, i and Supplementary Fig. 2g). The GO results also showed PSR-related pathways represented by m^{6}A-modified PSI genes, regardless of PSI-m^{6}A (Supplementary Fig. 2h, i).

Together, the above data show that Pi starvation induces global changes in m^{6}A levels. Many PSR-related transcripts were m^{6}A modified, suggesting that m^{6}A regulates Pi homeostasis and PSR signaling.

Increases in m^{6}A levels in PSR are largely mediated by PHRs

PHR1 and its homologs are central TFs controlling multiple processes of the PSR[47,48], raising the question of whether PSI-m^{6}A modifications are mediated by PHRs. To address this, we conducted m^{6}A-seq using the *phr1 phl1* double knockout mutant under normal (+P) and Pi-deficient (−P) conditions. We obtained high-quality and highly reproducible m^{6}A-seq and corresponding mRNA-seq data (used as Input) (Fig. 3a, b and Supplementary Fig. 3a, b). After systematic calibration with the non-m^{6}A IVT RNA libraries (Fig. 1a), approximately 11,000 high-confidence m^{6}A peaks were identified in the *phr1 phl1* double mutant under both +P and −P conditions (Supplementary Fig. 3c, d and Supplementary Data 1).

Clustering and principal component analysis (PCA) revealed distinct clustering patterns in the m^{6}A-seq data of WT and *phr1 phl1* between +P and −P conditions, with the *phr1 phl1* and WT clusters near each other under +P but distant both from each other and from the +P clusters under −P (Fig. 3a, b). These results highlight the dramatic difference in global m^{6}A modifications in WT and *phr1 phl1* plants under Pi starvation, but not under normal conditions. This finding was confirmed by transcriptome-wide differential m^{6}A modification analysis using the exomePeak algorithm. Under +P, the transcriptome-wide m^{6}A profiles of WT and *phr1 phl1* were comparable ($P = 0.88$, Wilcox test) (Fig. 3c), with fewer than 1000 differentially methylated m^{6}A peaks between the two genotypes (Supplementary Fig. 3e and

https://doi.org/10.1038/s41467-025-59331-y

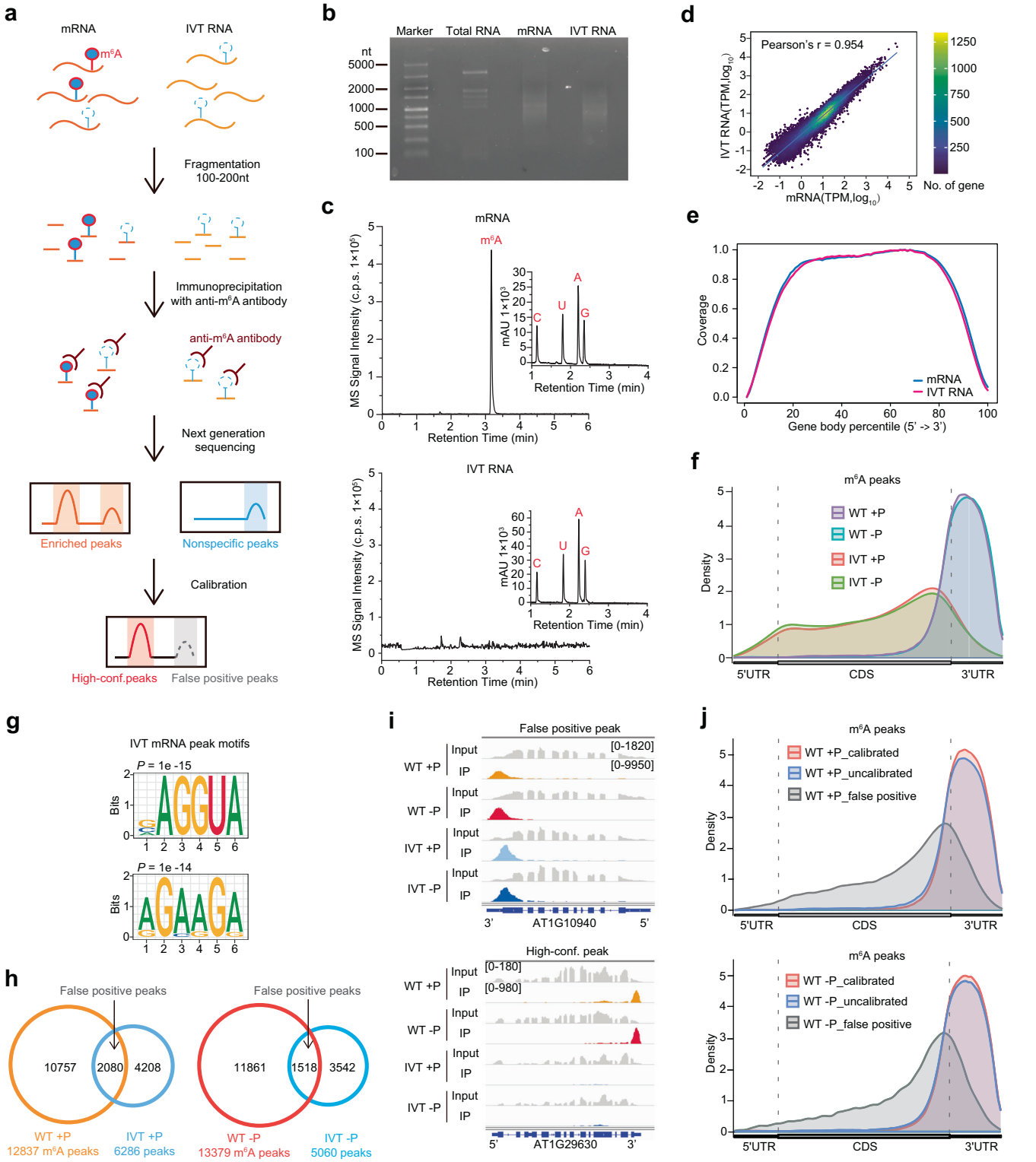

Fig. 1 | Transcriptome-wide high-confidence m⁶A profiling with systematic calibration. a Diagram of the systematic calibration process using a synthetic modification-free RNA library. **b** Gel image of total RNA, endogenous mRNA, and IVT RNA, showing a close resemblance between endogenous mRNA and IVT mRNA. This experiment was independently repeated once with similar results. **c** LC–MS/MS results showing that m⁶A modifications were not detected in IVT RNA. **d** Transcript levels showing a high correlation between endogenous mRNA and IVT RNA abundances. TPM, transcripts per million. **e** Metagene plot of read coverage from the 5′ end to the 3′ end of the transcripts, revealing the full-length coverage of IVT RNA. **f** Metagene profiles showing the distribution of peaks from the WT mRNA and IVT RNA m⁶A-seq samples. **g** Motif analysis of peaks identified from the IVT RNA m⁶A-seq data. *P* value was calculated using a one-tailed hypergeometric test. **h** Venn diagram showing the overlap of m⁶A peaks between the WT mRNA and the corresponding IVT RNA m⁶A-seq libraries under +P and −P conditions. Approximately 16% and 11% of m⁶A peaks of the +P and −P WT mRNA libraries, respectively, are false-positive peaks. **i** Cumulative reads for one representative gene locus of a false-positive peak and a high-confidence (High-conf.) m⁶A peak, respectively. 5′ and 3′ indicate the direction of the gene. **j** Metagene profiles showing the distribution of peaks of uncalibrated, calibrated, and false-positive peaks from the WT samples. The calibrated peaks show a sharper distribution than the uncalibrated peaks. Source data are provided as a Source Data file.

https://doi.org/10.1038/s41467-025-59331-y

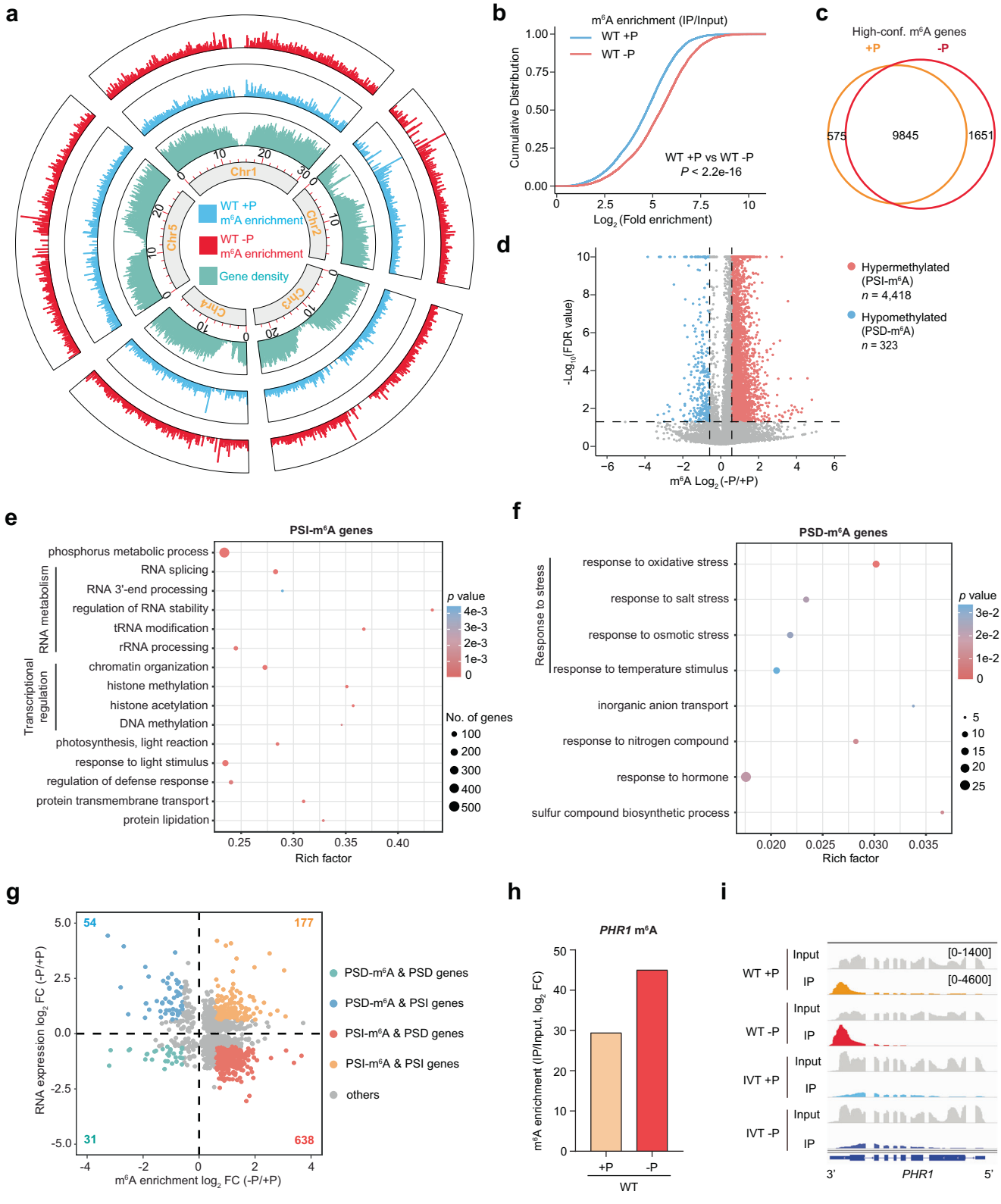

Supplementary Data 1). Under Pi starvation, however, the loss of *PHR1* and *PHL1* diminished the global increase in PSI-m^{6}A modifications observed in the WT ($P < 2.2e-16$, Wilcox test) (Fig. 3c). Under these conditions, the levels of 3265 m^{6}A peaks decreased (hypo-m^{6}A peaks, corresponding to 3194 hypo-m^{6}A genes), whereas the levels of only 477 m^{6}A peaks increased (hyper-m^{6}A peaks, corresponding to 465 hyper-m^{6}A genes) in *phr1 phl1* compared to the WT (Fig. 3d and Supplementary Data 1). Furthermore, approximately 60% of these hypo-m^{6}A peaks were represented in the PSI-m^{6}A peaks (hereafter PHR-mediated PSI-m^{6}A peaks) (Fig. 3e and Supplementary Data 1). Meanwhile, 70 hyper-m^{6}A peaks were PSD-m^{6}A peaks (hereafter, PHR-mediated PSD-m^{6}A peaks) (Fig. 3f and Supplementary Data 1), suggesting that the PHRs regulate the Pi starvation–triggered m^{6}A dynamics, mainly by mediating the induction of PSI-m^{6}A modifications. We further confirmed that the m^{6}A levels of these corresponding PHR-mediated PSI-m^{6}A genes significantly increased in response to Pi

https://doi.org/10.1038/s41467-025-59331-y

Fig. 2 | Pi starvation induces global m^{6}A modification. a Circos plot of the gene density and enrichment of the m^{6}A modification in WT m^{6}A-seq data under +P and −P conditions, showing that Pi starvation induces widespread m^{6}A modifications. **b** Cumulative curve of m^{6}A enrichment (IP/Input) in the WT under +P and −P conditions, showing a global induction of m^{6}A modification by Pi starvation. *P* value was calculated using a two-tailed Kolmogorov-Smirnov test. **c** Venn diagram showing the overlap of high-confidence (High-conf.) m^{6}A-modified genes between +P and −P. **d** Volcano plot of m^{6}A enrichment with over 4000 hypermethylated m^{6}A peaks and ~300 hypomethylated m^{6}A peaks under −P compared with +P conditions. PSI-m^{6}A, Pi starvation–induced m^{6}A peaks; PSD-m^{6}A, Pi starvation–decreased m^{6}A peaks. FDR value was calculated using a one-tailed rescaled hypergeometric test. **e**, **f** GO analysis of PSI-m^{6}A genes (**e**) and PSD-m^{6}A genes (**f**). *P* value was calculated using a one-tailed hypergeometric test. **g** Joint analysis of m^{6}A-seq and RNA-seq data in the WT revealing the preferential deposition of PSI-m^{6}A modifications on PSD genes. Differentially expressed genes (fold change ≥ 1.5 and $P < 0.05$) with differentially methylated m^{6}A peaks (fold change ≥ 1.5 and FDR < 0.05) are highlighted in different colors. The numbers of the indicated gene groups are shown. *P* value was calculated using an unpaired two-tailed Student's *t*-test; FDR value was calculated using a one-tailed rescaled hypergeometric test. **h**, **i** Bar graph (**h**) and IGV view (**i**) of the PSI-m^{6}A modifications on *PHR1* transcripts. Source data are provided as a Source Data file.

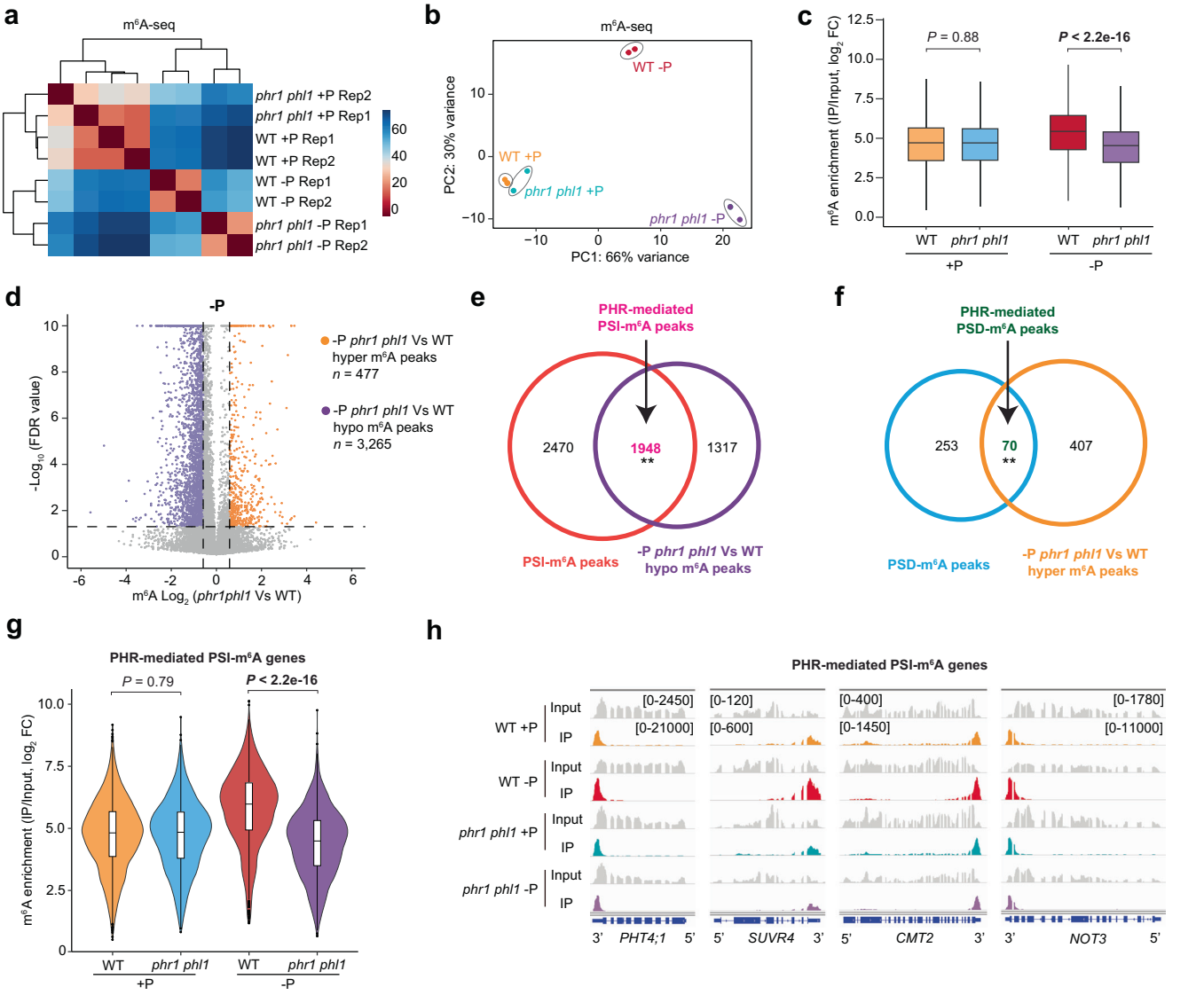

Fig. 3 | Pi starvation–induced m^{6}A modifications are largely mediated by PHRs. a, **b** m^{6}A-seq clustering (**a**) and principal component analysis (PCA) (**b**) confirming the high reproducibility between biological replicates and the differences between the WT and *phr1 phl1* samples under −P but not +P conditions. **c** Box plots showing a significant decrease in m^{6}A modification levels in *phr1 phl1* compared with the WT under −P but not +P conditions. +P WT, $n = 11{,}472$; +P *phr1phl1*, $n = 11{,}923$; −P WT, $n = 12{,}513$; −P *phr1phl1*, $n = 12{,}378$. **d** Volcano plot of m^{6}A enrichment, with 3265 hypomethylated m^{6}A peaks and 477 hypermethylated m^{6}A peaks in *phr1 phl1* compared with the WT under −P conditions. FDR value was calculated using a one-tailed rescaled hypergeometric test. **e**, **f** Venn diagrams showing PHR-mediated PSI-m^{6}A peaks ($P = 0$) (**e**) and PHR-mediated PSD-m^{6}A peaks ($P = 1.90e\text{-}49$) (**f**). $^{**}P < 0.01$, the one-tailed hypergeometric test. **g** Violin plots showing a significant decrease in m^{6}A modifications of PHR-mediated PSI-m^{6}A genes ($n = 1931$) in *phr1 phl1* compared with the WT under −P but not +P conditions. **h** IGV view of the m^{6}A-seq signals of selected PHR-mediated PSI-m^{6}A genes. In (**c** and **g**), *P* values were calculated using the two-tailed Wilcoxon test. The midlines and box edges indicate the medians and quartiles, respectively. The whiskers extend to the farthest data point within 1.5 times the interquartile range (IQR) from the box edges.

starvation stress in the WT, but not in *phr1 phl1* (Fig. 3g, h). Notably, m^{6}A induction of both total PSI-m^{6}A and non-PHR-mediated PSI-m^{6}A genes was also significantly repressed in *phr1 phl1* compared with the WT under −P conditions, indicating that PHRs mediated global PSI-m^{6}A modifications (Supplementary Fig. 3f, g). Consistent with the GO results for the PSI-m^{6}A genes (Fig. 2e), GO analysis of the PHR-mediated PSI-m^{6}A genes and non-PHR-mediated PSI-m^{6}A genes revealed their involvement in phosphorus metabolism, RNA splicing, RNA stability, chromatin remodeling, photosynthesis, and protein transport, among other functions (Supplementary Fig. 3h, i).

These results indicate that the PSI-m^{6}A modifications are dependent on PHRs, suggesting a new role of PHR proteins in regulating the PSR via m^{6}A modification.

PHRs do not mediate PSI-m^{6}A modification through direct transcriptional regulation

The PHR TFs regulate the expression of many PSI genes[53]; thus, we investigated whether the PHRs mediate the m^{6}A levels of these PSI-m^{6}A transcripts via the direct transcriptional regulation of these genes. We first compared the PHR-mediated PSI-m^{6}A genes with direct target genes of PHR1 that were previously identified using chromatin immunoprecipitation (ChIP)-seq[73]. Only 155 of the PHR-mediated PSI-m^{6}A genes (accounting for 8% of the total) overlapped with the direct target genes of PHR1 (accounting for 7% of the total) (Supplementary Fig. 4a), indicating that the PHR1-mediated regulation of PSI-m^{6}A modifications is mainly achieved via a mechanism other than direct transcriptional regulation. To further explore this idea, we compared our RNA-seq data from WT and *phr1 phl1*. More than half of the PSI genes (~ 51%) were repressed (classified as PHR-controlled PSI genes), while only ~15% of PSD genes were upregulated (classified as PHR-controlled PSD genes) in *phr1 phl1* compared with the WT under −P conditions (Supplementary Fig. 4b, c and Supplementary Data 2). This is consistent with the previous finding that PHRs mainly transcriptionally regulate the induction of PSI genes under −P conditions[53]. However, only 34 of the PHR-mediated PSI-m^{6}A genes (accounting for 2% of the total) overlapped with the PHR-controlled PSI genes (accounting for 3% of the total) (Supplementary Fig. 4d), confirming the notion that PHRs do not transcriptionally regulate PHR-mediated PSI-m^{6}A genes.

In addition, we measured the expression levels of genes encoding m^{6}A writers (*MTA*, *MTB*, *FIP37*, *VIR*, *HAKAI*, and *FIONA1*) and erasers (*ALKBH9B* and *ALKBH10B*) in the WT and *phr1 phl1* under +P and −P conditions. The expression of these genes was not greatly altered in response to Pi-deficiency or the mutation of *PHR1* and *PHL1* (Supplementary Fig. 4e). We further detected the protein levels of MTA in the WT and *phr1 phl1* mutants under +P and −P but found no obvious changes in total proteins (Supplementary Fig. 4f). Besides, the amount of MTA and MTB proteins in nuclei was comparable with the WT between +P and −P conditions (Supplementary Fig. 4g).

Taken together, these data demonstrate that PHRs mediate PSI-m^{6}A modifications, but not via either direct transcriptional regulation or protein abundance changes of m^{6}A writers, pointing to the involvement of an unknown regulatory mechanism.

PHR1 interacts with MTA and MTB in nuclei under Pi starvation conditions

Several factors interact with m^{6}A writers to regulate miRNA biogenesis[74,75], the circadian clock[76] and chlorophyll homeostasis[77]. Using yeast two-hybrid (Y2H) assays, we observed the interactions of PHR1 with MTA and MTB, but not with FIP37, another component of the core m^{6}A methyltransferase complex (MTC) (Fig. 4a). Meanwhile, SPX1 and SPX2, which are repressors of PHR activity, did not interact with any MTC component in the Y2H system (Fig. 4b). To confirm the in vivo interaction between PHR1 and MTA/MTB, we performed bimolecular fluorescence complementation (BiFC) assays (Fig. 4c). PHR1 interacted with MTA and MTB in the nucleus, and they formed speckles in some cells (Fig. 4c). These results are consistent with reports of condensate formation by the MTC[74,75]. Furthermore, we validated the PHR1-MTA/MTB interaction in plants under −P conditions by nuclear Co-IP (Fig. 2d).

These results elucidated the association of PHR1 with MTA and MTB under −P conditions in plants. Given the current data obtained under −P conditions in plants, it appears that PHR1, a key transcription factor in the PSR, plays a previously unrecognized role in regulating PSI-m^{6}A under −P, possibly through interacting with MTA and MTB.

m^{6}A RNA modification facilitates Pi homeostasis and systemic PSR signaling

To further decipher the roles of m^{6}A modification in Pi homeostasis and PSR signaling, we developed a line hypomorphic for the m^{6}A writer gene *MTA* using the artificial microRNA method (*amiR-mta*) (Fig. 5a and Supplementary Fig. 5a). The expression level of *MTA* in *amiR-mta* was repressed to ~25% that of WT plants (Fig. 5f and Supplementary Fig. 5b). We quantified the global m^{6}A level in *amiR-mta* using LC–MS/MS, revealing a dramatic reduction in the m^{6}A/A ratio compared with the WT (decreased to ~40%) under both +P and −P conditions (Supplementary Fig. 5c).

The *amiR-mta* plants exhibited inhibited growth under +P conditions, with reduced biomass and shorter primary roots, which is consistent with previous findings (Fig. 5a–c)[10,13]. Under −P stress, this growth inhibition of *amiR-mta* was deteriorated (Fig. 5a–c). We then investigated the Pi homeostasis- and PSR-related physiological traits of the WT and *amiR-mta*. Compared with the WT, the knockdown of *MTA* resulted in a significant reduction in the shoot Pi concentration under both +P and −P conditions, indicating that the m^{6}A modification plays a positive role in Pi homeostasis (Fig. 5d). In addition, the inhibition of primary root growth is an important trait of the local PSR[47,69]. The ratio of primary root length under −P vs. +P conditions was slightly smaller in *amiR-mta* than in the WT, suggesting that the m^{6}A modification moderately represses the local PSR (Fig. 5e). These physiological phenotypes caused by the knockdown of the m^{6}A writer gene *MTA* provide further evidence that m^{6}A modifications play a regulation role in Pi homeostasis and the PSR.

We further explored the involvement of the m^{6}A modification in PHR-mediated systemic PSR signaling. We used RT-qPCR to assess the steady-state transcript levels of several systemic PSR-signaling genes, including *PHR1* and the downstream Pi transport- and Pi metabolism-related PSI genes. The steady-state transcript levels of *PHR1*, *PHF1*, *PHO1*, *PHT1;1/PT1*, and *ACID PHOSPHATASE 5* (*ACP5*) showed moderate but significant reductions in *amiR-mta* compared with the WT under −P (Fig. 5f). This is consistent with the reduced Pi concentration of *amiR-mta* plants (Fig. 5d). To further investigate the enhanced functions of m^{6}A modifications in PSR and Pi homeostasis in plants under −P conditions, we treated 7-day-old WT plants grown under normal conditions with the chemical STM2457, an inhibitor of m^{6}A writers[78] for 7 days under −P stress. Compared with 14-day-old WT plants grown under normal conditions, both STM2457-treated and mock WT plants exhibited typical morphological responses under Pi deficiency, such as inhibited primary root growth and anthocyanin accumulation (Supplementary Fig. 5d). Notably, the Pi concentration in shoots was lower in STM2457-treated WT plants than in mock plants under −P conditions (Supplementary Fig. 5e). Moreover, the expression levels of *PHR1* and its downstream PSR signaling genes *ACP5* and *PHF1* were lower in STM2457-treated WT plants compared with mock plants (Supplementary Fig. 5f). These results support the hypothesis that m^{6}A modifications positively regulate Pi homeostasis and PHR-mediated systemic PSR signaling in plants under Pi-deficiency stress.

We next profiled the transcriptomes of *amiR-mta* plants under +P and −P conditions to confirm the positive role of m^{6}A in PSR signaling. The knockdown of *MTA* dramatically altered the transcriptome, 1905

https://doi.org/10.1038/s41467-025-59331-y

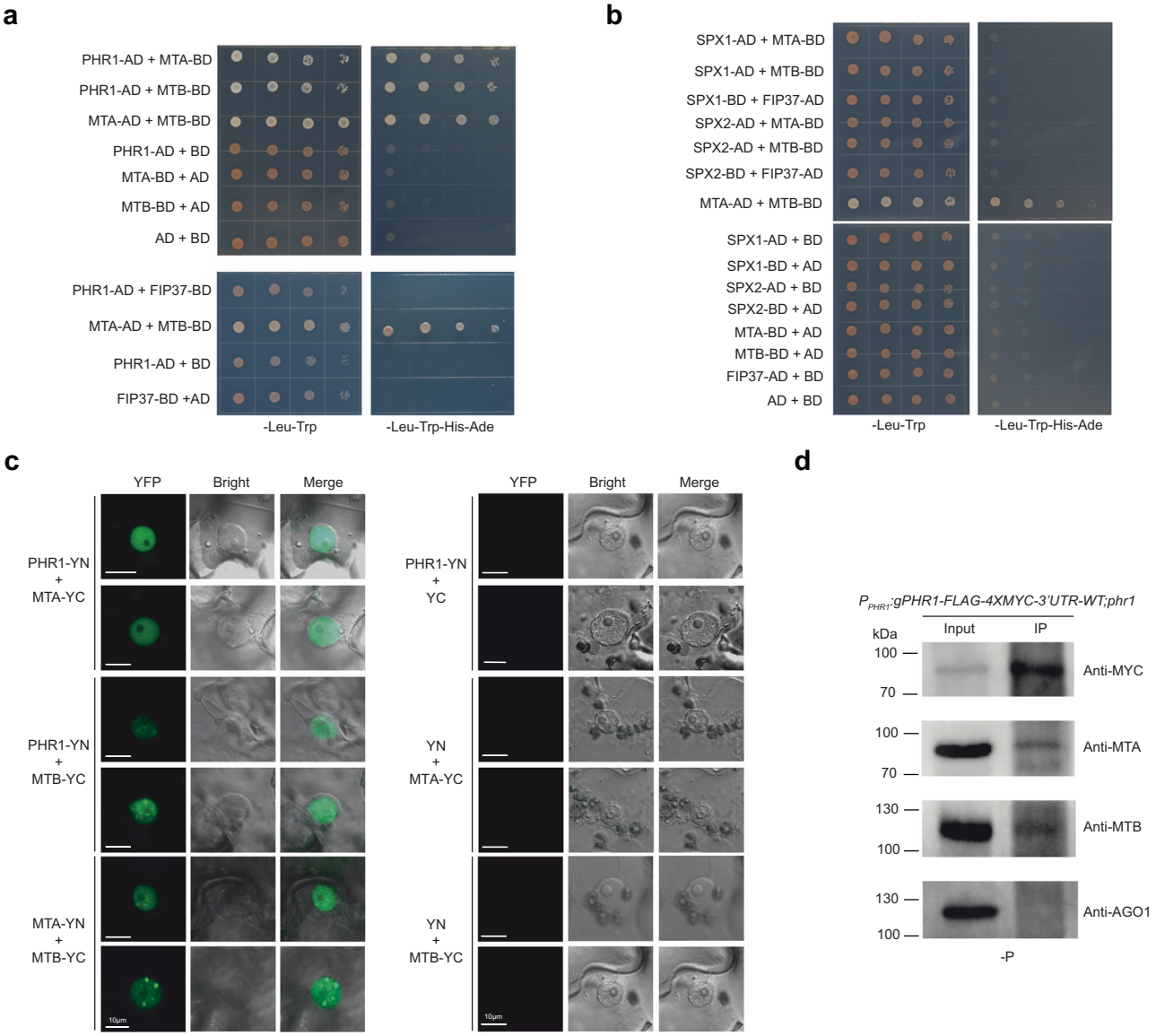

Fig. 4 | PHR1 interacts with MTA/MTB in the nucleus under −P conditions. a Y2H assay showing the interaction of PHR1 with MTA and MTB, but not FIP37. **b** Y2H assay showing that SPX1 and SPX2 do not interact with MTA, MTB, or FIP37. In (**a**, **b**), 1:10 serial dilutions are shown. The interaction between MTA and MTB served as a positive control. **c** BiFC assays showing the interaction of PHR1 with MTA and MTB in the nucleus. The interaction between MTA and MTB served as a positive control. Bars = 10 μm. **d** Nuclear Co-IP revealing the interaction of PHR1 with MTA and MTB under −P conditions. AGO1 served as a non-interacting control. The BiFC and nuclear Co-IP experiments were independently repeated once with similar results. Source data are provided as a Source Data file.

genes were upregulated and 1649 genes were downregulated in *amiR-mta* compared with the WT under +P conditions, and 2258 genes were upregulated and 1764 genes were downregulated in *amiR-mta* compared with WT under −P conditions (Supplementary Fig. 5g, h and Supplementary Data 2), suggesting that m^{6}A has a pronounced effect on RNA expression. We then examined the effect of m^{6}A on the abundance of PSR transcripts. Under +P conditions, only a small proportion of PSI and PSD genes were significantly upregulated (7.1% of PSI and 13.1% of PSD) or downregulated (13.1% of PSI and 4.6% of PSD) by the knockdown of *MTA* (Supplementary Fig. 5i). However, under −P conditions, *MTA* knockdown significantly upregulated a large proportion (30.8%) of PSD genes, while significantly downregulating a large proportion (21.4%) of PSI genes (Supplementary Fig. 5j). Further analysis showed that the PSI and PSD transcript levels were comparable between the WT and *amiR-mta* under +P conditions (Fig. 5g, h); however, under −P conditions, the upregulation of PSI genes and the downregulation of PSD genes were significantly attenuated in *amiR-mta* compared with the WT (Fig. 5g, h). These RT-qPCR and RNA-seq results provide further evidence that m^{6}A facilitates systemic PSR signaling, including both PSI and PSD signaling.

Taken together, the physiological and molecular phenotypes of *amiR-mta*, with its globally reduced m^{6}A levels, demonstrate that the m^{6}A modification promotes Pi homeostasis and systemic PSR signaling.

Regulation of transcriptome-wide RNA stability in response to Pi limitation

The finding that the m^{6}A RNA modification regulates RNA stability[1–3] and that it also alters the transcript abundance of PSR signaling genes (Fig. 5g, h) prompted us to investigate whether the m^{6}A modification also facilitates PSR signaling via its effects on RNA stability. We carried out a genome-wide mRNA decay assay using WT and *amiR-mta* plants under +P and −P conditions. We infiltrated the seedlings with the transcriptional inhibitor cordycepin and collected samples after 0, 15, 30, 60, and 120 min for RNA-seq analysis (Fig. 6a, see "Methods")[79].

https://doi.org/10.1038/s41467-025-59331-y

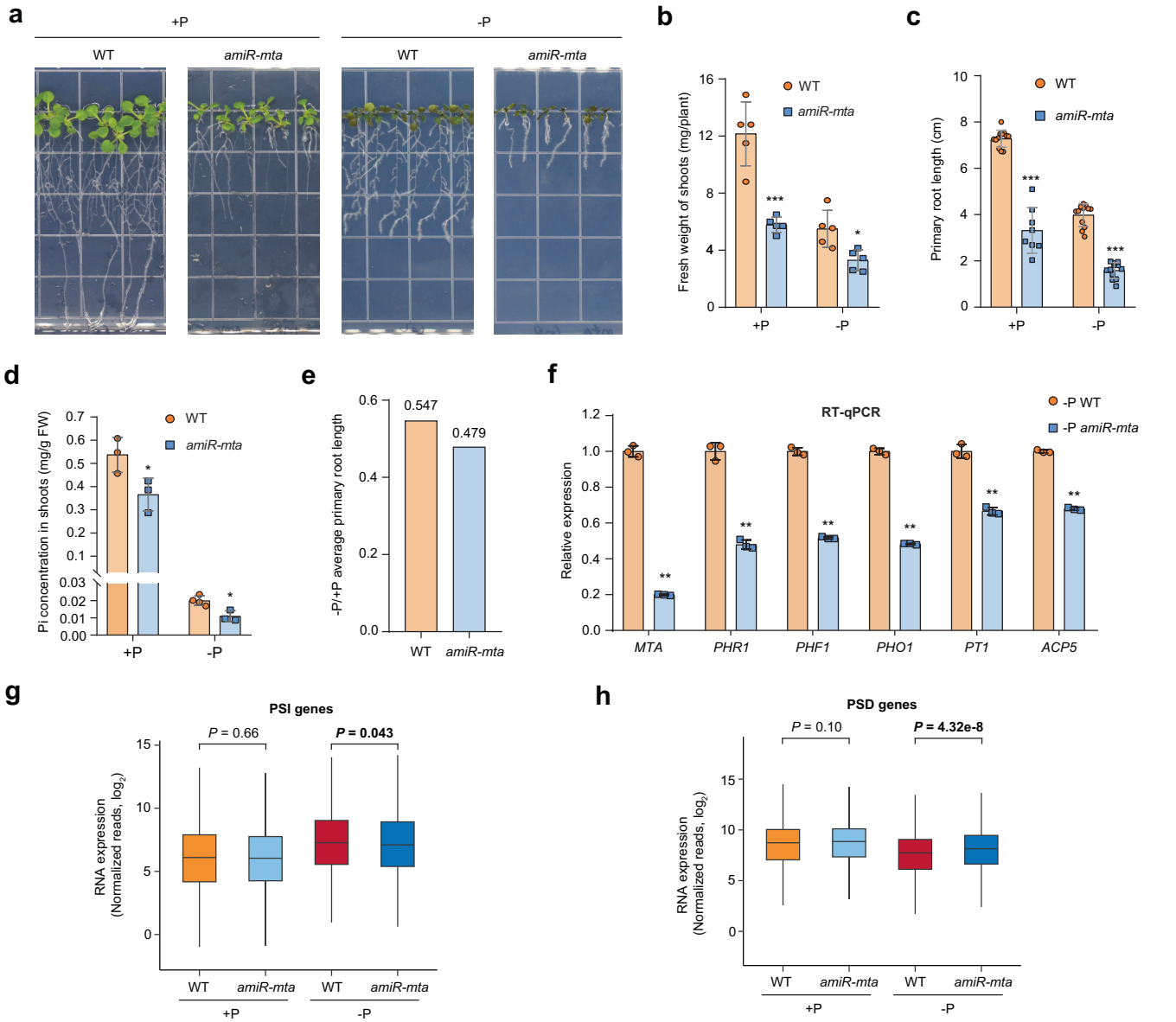

Fig. 5 | m^{6}A modification promotes Pi homeostasis and systemic PSR signaling. **a** Images of 14-day-old WT and *amiR-mta* seedlings after seven days of growth under normal (+P) and Pi-deficient (−P) conditions. **b**–**d** Fresh weight of shoots ($n = 5$ biological replicates) (**b**), primary root length ($n = 8$ individual plants for +P *amiR-mta*, $n = 12$ individual plants for others) (**c**), and Pi concentration in the shoots ($n = 4$ biological replicates for −P WT, n = three biological replicates for others) (**d**) of WT and *amiR-mta* under +P and −P conditions. **e** The ratio of average primary root length in WT and *amiR-mta* seedlings under −P conditions relative to the length under +P conditions. The exact values of the ratio were shown. **f** RT-qPCR showing significantly reduced expression of *PHR1* and its downstream PSI genes in *amiR-mta* compared with WT under −P conditions. The relative expression levels of genes were normalized to those of −P WT, where the ratio was arbitrarily set to 1 with SD calculated from three biological repeats. **g**, **h** Transcriptome-wide RNA-seq data showing significantly reduced expression of PSI genes ($n = 2112$) (**g**) and significantly increased expression of PSD genes ($n = 1888$) (**h**) in *amiR-mta* compared with WT under −P but not +P conditions. *P* values were calculated using the two-tailed Wilcoxon test. The midlines and box edges indicate the medians and quartiles, respectively. The whiskers extend to the farthest data point within 1.5 times the interquartile range (IQR) from the box edges. In (**b**–**d** and **f**), data are presented as mean values ± SD; $^*P < 0.05$; $^{**}P < 0.01$; $^{***}P < 0.001$, as determined using an unpaired two-tailed Student's *t*-test. Source data are provided as a Source Data file.

Three biological replicates were sequenced and generated highly reproducible data (Supplementary Fig. 6a). Following data normalization and the exclusion of low-abundance mRNAs, we used transcript levels to model the decay rates for each gene (see Methods)[79].

We first benchmarked the fidelity of our RNA decay data. The previously reported unstable gene AT4G25490[79] was confirmed to have a short half-life ($t_{1/2}$) in our analysis ($t_{1/2} = 4.44$ min under +P and 6.86 min under −P). Next, we randomly chose six genes with short, medium, and long half-lives (two genes each) under both +P and −P conditions and confirmed their RNA stabilities using RT-qPCR (Supplementary Fig. 6b). All tested genes exhibited a similar RNA decay pattern in both transcriptome-wide RNA decay analysis and target-specific RT-qPCR (Supplementary Fig. 6b, c). We then examined the decay rates of *PHOSPHATE2* (*PHO2*) transcripts, which are known to be cleaved by miR399 and are therefore thought to have a shorter half-life under −P than under +P[80,81]. Indeed, the *PHO2* transcripts exhibited a shorter half-life in the −P samples than in the +P samples (Fig. 6b). These results demonstrate the high fidelity and quality of our transcriptome-wide RNA decay data.

We then evaluated the transcriptome-wide changes in RNA stability mediated by Pi starvation. In the WT, the half-lives of approximate 56% of genes were altered under −P treatment compared with

https://doi.org/10.1038/s41467-025-59331-y

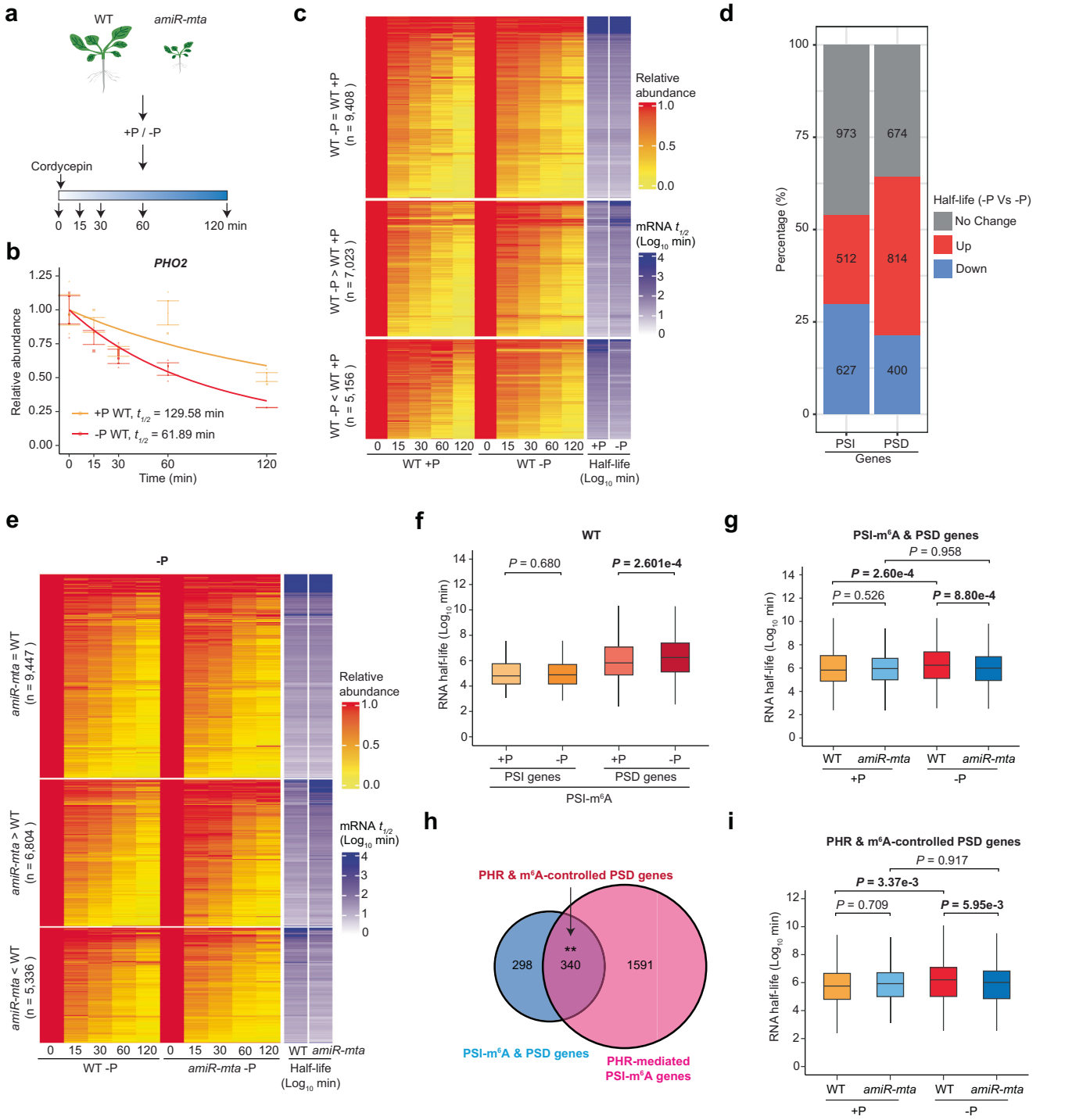

Fig. 6 | PSI-m^{6}A feedback enhances the RNA stability of PSD genes. a Diagram of genome-wide RNA decay analysis. **b** Profile of *PHO2* transcript decay in the WT under +P and −P conditions. The relative *PHO2* mRNA abundance following the inhibition of transcription is shown, with bars indicating the means ± SE, $n = 3$; thick lines indicate modeled values. The half-life ($t_{1/2}$) of *PHO2* mRNA is indicated for each treatment. **c** Heatmap of RNA decay over 120 min in the WT under +P and −P conditions, revealing that more than half of the transcripts show altered half-lives under Pi starvation. **d** The half-lives of over half of PSI and PSD genes are altered by Pi starvation. The number of genes in each category is shown. **e** Heatmap of RNA decay over 120 min in the WT and *amiR-mta* under −P conditions, revealing that more than half of the transcripts show altered half-lives in *amiR-mta* compared to the WT under −P conditions. **f** The half-lives of the m^{6}A-hypermethylated PSD genes (PSI-m^{6}A & PSD genes) significantly increase upon Pi starvation (−P) compared with +P in the WT. PSI-m^{6}A & PSI genes, $n = 177$; PSI-m^{6}A & PSD genes, $n = 638$. **g** The −P-induced half-lives of the PSI-m^{6}A & PSD genes ($n = 638$) are diminished in *amiR-mta* compared with the WT. **h** Venn diagram showing a significant overlap between PSI-m^{6}A & PSD genes and PHR-mediated PSI-m^{6}A genes. $^{**}P < 0.01$; $P = 4.07e\text{-}188$ for the one-tailed hypergeometric test. **i** The −P-induced half-lives of the PHR & m^{6}A-controlled PSD genes ($n = 340$) are diminished in *amiR-mta* compared with the WT under −P. In (**c** and **e**), the heatmap hierarchically clusters 21,587 transcripts into three groups, as indicated. RNA decay quantification is presented as the change in mean relative to the RNA abundance and RNA half-life ($t_{1/2}$). In (**f**, **g**, and **i**), the *P* values were calculated using the two-tailed Wilcoxon test. The midlines and box edges indicate the medians and quartiles, respectively. The whiskers extend to the farthest data point within 1.5 times the IQR from the box edges. Source data are provided as a Source Data file.

the +P control (Fig. 6c), with approximately 7000 genes having a prolonged half-life and 5000 genes having a shorter half-life under Pi starvation (Fig. 6c and Supplementary Data 3). These results point to an additional layer of PSR regulation through the RNA decay pathway. Of the PSR-signaling genes examined, approximately 54% of PSI genes and 64% of PSD genes showed altered RNA stability under Pi starvation (Fig. 6d). We noticed that more than half (~55%) of PSI genes with altered RNA stability had decreased half-lives, whereas the majority (~67%) of PSD genes with altered RNA stability had longer half-lives (Fig. 6d). The opposite trends in RNA levels and RNA stability in response to Pi starvation indicated the existence of the feedback regulation of RNA stability for certain PSR genes.

Feedback regulation of PSI-m^{6}A promotes the stability of PSD gene transcripts

We next evaluated whether PSI-m^{6}A modifications participate in regulating the stability of PSR transcripts. We compared RNA half-life data from WT and *amiR-mta* plants. Under +P conditions, the RNA half-life of the majority of genes was higher in *amiR-mta* compared with the WT, with 11,193 genes showing a longer half-life and 2965 genes showing a shorter half-life in the *amiR-mta* plants (Supplementary Fig. 7 and Supplementary Data 3). These results suggest that m^{6}A plays dual roles in RNA stability and that m^{6}A modifications mainly destabilize transcripts under normal conditions. Moreover, the half-lives of both m^{6}A-methylated and non-m^{6}A-methylated transcripts increased globally in *amiR-mta* under +P conditions, indicating that m^{6}A negatively regulates global RNA stability in both direct and indirect manners (Supplementary Fig. 7d).

Unexpectedly, under −P conditions, the RNA half-life did not exhibit a dramatic global increase in *amiR-mta* compared to the WT (Supplementary Fig. 7a). A detailed analysis showed that 6804 and 5336 genes had increased and decreased half-lives, respectively (Fig. 6e and Supplementary Data 3). The positive effect of m^{6}A on RNA stability appears to be enhanced under −P conditions. We examined the RNA stability of the −P-mediated m^{6}A-hypermethylated PSR genes. The half-lives of m^{6}A-hypermethylated PSD genes (PSI-m^{6}A & PSD genes), but not m^{6}A-hypermethylated PSI genes (PSI-m^{6}A & PSI genes), significantly increased under −P compared to control conditions (+P), indicating that PSI-m^{6}A-mediated feedback enhances the RNA stability of m^{6}A-hypermethylated PSD transcripts (Fig. 6f). Furthermore, this increased RNA stability of −P-induced m^{6}A-hypermethylated PSD genes was repressed in *amiR-mta* plants (with dramatically reduced m^{6}A levels of global and PSI-m^{6}A & PSD genes [Supplementary Fig. 8a, b]) compared with the WT under −P but not +P conditions, confirming the positive role of PSI-m^{6}A in the RNA stability of PSD genes (Fig. 6g). Moreover, more than half of these m^{6}A-hypermethylated PSD genes were also PHR-mediated PSI-m^{6}A genes (Fig. 6h). We named these overlapping genes PHR & m^{6}A-controlled PSD genes (Supplementary Data 1). The half-lives of the PHR & m^{6}A-controlled PSD genes also increased in response to Pi starvation in the WT but not in *amiR-mta* plants (Fig. 6i), indicating that feedback regulation of the PHRs fine-tunes the expression of some PSD genes via m^{6}A-mediated mRNA stabilization.

Taken together, our transcriptome-wide RNA stability profiling of WT and *amiR-mta* plants under +P and −P conditions, as well as the m^{6}A landscape in *miR-mta* under −P conditions, revealed a new layer of PSR regulation at the level of RNA stability. Moreover, this analysis revealed that PHR-mediated Pi starvation–induced m^{6}A feedback extends the RNA half-lives of PSD genes.

PSI-m^{6}A does not facilitate RNA stability through APA shifts

It has been reported that m^{6}A could affect RNA stability via APA shifts[26,82]. To investigate whether PSI-m^{6}A facilitates RNA stability via APA shifts, we performed PAS-seq 2[83] to profile APA sites on a transcriptome-wide level under +P and −P conditions in WT and *amiR-mta* seedlings. PCA revealed high reproducibility among three biological replicates of each sample (Supplementary Fig. 9a). Moreover, most poly(A) tags (PATs) aligned to the 3′UTRs of protein-coding genes (~70%) (Supplementary Fig. 9b). These results reflect the high quality of our PAS-seq 2 data.

Following previous studies[82,84], we assigned adjacent PATs within a 24-nt window to PAS clusters (PACs). In total, 71,753 PACs (corresponding to 17,968 genes) were detected in WT and *amiR-mta* under −P and +P conditions. Furthermore, we compared the PAC shift events between the WT and *amiR-mta*. Under both +P and −P conditions, the knockdown of *MTA* led to dramatic PAC shifts (Supplementary Fig. 9c). Specifically, 2463 significant distal-to-proximal shifts (hereafter d2p) and 461 significant proximal-to-distal shifts (hereafter p2d) were detected under +P conditions and 1992 significant d2p and 397 significant p2d events were detected under −P conditions in *amiR-mta* compared with the WT (Supplementary Fig. 9c and Supplementary Data 4). This observation is also similar to the results for the m^{6}A reader mutant *cpsf30-l* (*cleavage and polyadenylation specificity factor 30 long-isoform*)[82]. Approximately 54% of d2p-shifted genes (total of 1222) and 14% of p2d-shifted genes (total of 657) in *cpsf30-l* are also shifted in *amiR-mta* (Supplementary Fig. 9d). These results support the role of m^{6}A modifications in regulating APA.

Next, we investigated the −P-induced PAC shifts in WT. We identified 203 significant d2p and 189 significant p2d events under −P compared with +P in the WT, pointing to the potential regulation of APA shifts in response to Pi deficiency (Supplementary Fig. 9c and Supplementary Data 4). Approximately half of these PSR APA-shifted genes were accompanied by changes in RNA stability (Supplementary Fig. 9e). We compared these PSR $t_{1/2}$-altered and APA-shifted genes with PSR m^{6}A-altered genes. We observed a non-significant overlap of PSI-m^{6}A and PSD-m^{6}A genes with PSR $t_{1/2}$-altered d2p-shifted and p2d-shifted genes (Supplementary Fig. 9f). These overlapping genes only accounted for ~1% of PSI-m^{6}A genes, indicating that the effects of PSI-m^{6}A modifications on RNA stability are not due mainly to APA shifts (Supplementary Fig. 9f). Meanwhile, the APA of only 18.5% of PSI-m^{6}A & PSD genes was altered in *amiR-mta* compared with WT under −P conditions (Supplementary Fig. 9g). Moreover, APA shift and IGV analysis showed that the APA of *PHR1* transcripts was not obviously shifted in the WT or *amiR-mta* under +P or −P conditions (Supplementary Fig. 9h).

Our results showed a potential regulation in APA shifts in response to Pi deficiency, but the PSI-m^{6}A-induced increase in RNA stability is not due to shifts in APA.

PSI-m^{6}A modification stabilizes *PHR1* mRNA to facilitate PSI signaling

We noticed that the global half-life of the m^{6}A-hypermethylated PSI transcripts was unaffected by either Pi starvation or the knockdown of *MTA* (Fig. 6f and Supplementary Fig. 10), whereas the global expression of PSI genes was reduced in *amiR-mta* (Fig. 5g). Given that PSI-m^{6}A modifications occurred on the transcripts of *PHR1*, encoding a master regulator of PSI signaling (Fig. 2g–i) and that its half-life and m^{6}A level was reduced in *amiR-mta* compared with the WT under −P (Fig. 7a and Supplementary Fig. 8c), we hypothesized that PSI-m^{6}A stabilizes *PHR1* mRNA to facilitate the expression of PSI genes under −P conditions.

To explore this hypothesis, we mutated putative m^{6}A modification loci (mutation from A to U) in the 3′ UTR of *PHR1* and expressed this mutant gene in the *phr1* null mutant background (P_{PHR1}*:gPHR1-FLAG-4XMYC-3UTR-MUT; phr1*, hereafter *PHR1-MUT*), with the WT variant serving as the control (P_{PHR1}*:gPHR1-FLAG-4XMYC-3UTR-WT; phr1*, hereafter *PHR1-WT*) (Fig. 7b). The 3′ UTR of *PHR1* contains seven putative m^{6}A loci, including one RRACH motif, two plant-specific UGUA motif, and four newly identified CAGR motifs (Fig. 7b and Supplementary Fig. 1e). UGUA and CAGR motifs are also enriched in 3′ UTR-located PSI-m^{6}A genes (Supplementary Fig. 2d). Six of these seven

https://doi.org/10.1038/s41467-025-59331-y

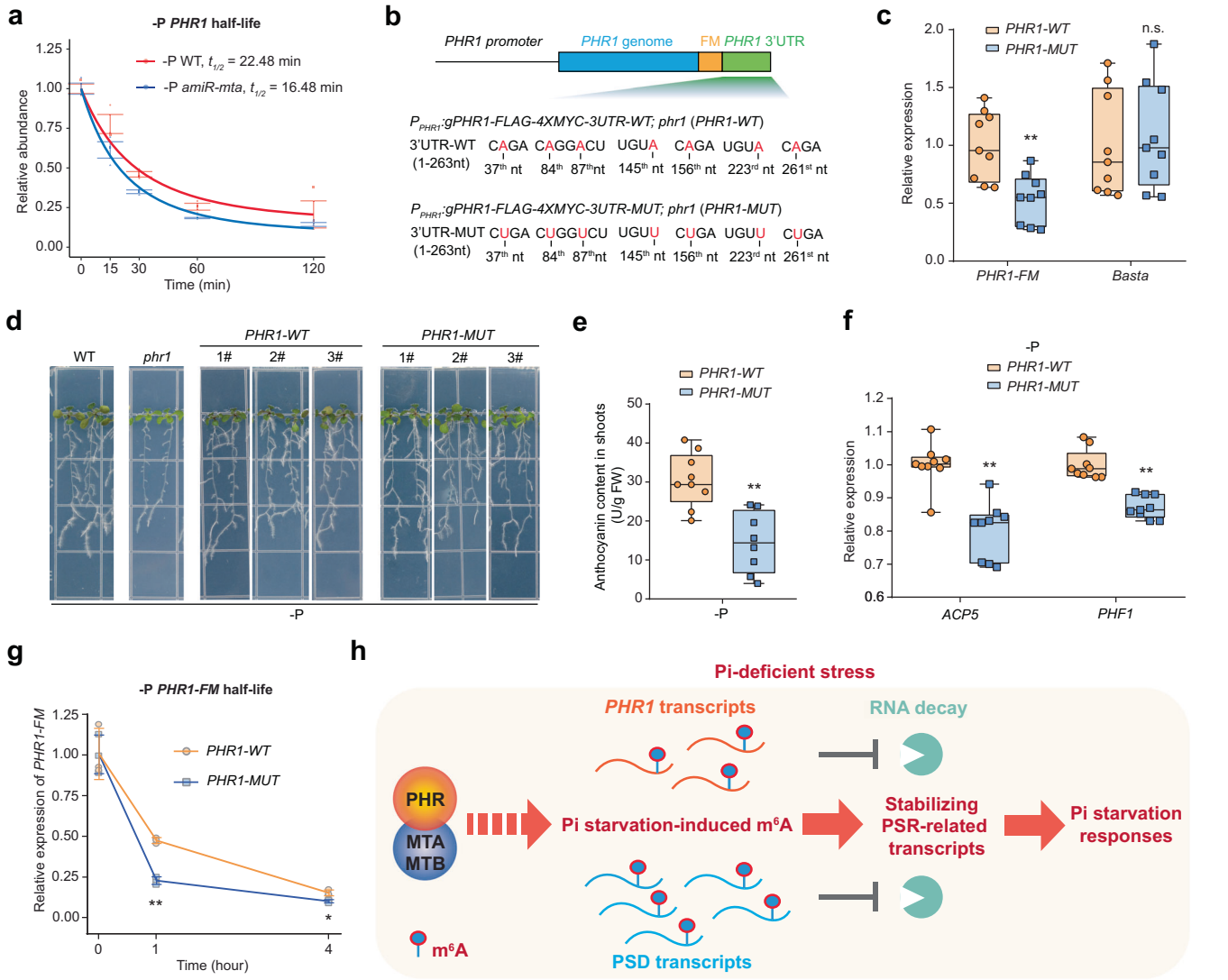

Fig. 7 | PSI-m^{6}A stabilizes *PHR1* transcripts to facilitate PSI signaling. a Profile of *PHR1* transcript decay showing its decreased half-life in *amiR-mta* compared with the WT under −P conditions. The relative RNA abundance following the inhibition of transcription is shown, with bars indicating the means ± SE, $n = 3$; thick lines indicate modeled values. The half-life ($t_{1/2}$) of *PHR1* is indicated for each genotype. **b** Diagram of self-promoter-driven and Flag-4Myc (FM)-tagged genomic *PHR1* with WT and m^{6}A-loci-mutated 3′ UTR. The seven putative m^{6}A loci and corresponding mutants are shown. The numbers indicate the positions of the mutated A, counted from the first nucleotide of the 3′ UTR. **c** *PHR1-FM* expression is significantly reduced in *PHR1-MUT* compared to *PHR1-WT* transgenic plants, while the expression of the control gene *Basta* is unchanged. **d** Images of 14-day-old WT, *phr1*, *PHR1-WT*, and *PHR1-MUT* seedlings after seven days of growth under Pi-deficient conditions (−P). The *PHR1-MUT* and *phr1* mutant, but not *PHR1-WT*, accumulated less anthocyanin than the WT. **e** Anthocyanin contents in *PHR1-MUT* and *PHR1-WT* shoots under −P conditions. **f** RT-qPCR analysis of the expression of genes downstream of PHR1 (*ACP5* and *PHF1*) in *PHR1-MUT* and *PHR1-WT* under −P conditions. **g** Target-specific RNA decay of the half-life of *PHR1-FM* in *PHR1-MUT* and *PHR1-WT* under −P conditions. The relative expression levels of transcripts were normalized to those at the 0 h time point, where the ratio was arbitrarily set to 1 with SD calculated from three biological repeats. **h** Model of the role of PHR-mediated PSI-m^{6}A modifications in stabilizing PSR-related transcripts to facilitate plant adaptation to stress. In (**c**, **e**, **f**, and **g**), $^*P < 0.05$; $^{**}P < 0.01$, as determined using an unpaired two-tailed Student's *t*-test; n.s. indicates not significant. In (**c**, **e**, **f**), the midlines and box edges indicate the medians and quartiles, respectively. The whiskers extend to the farthest data point within 1.5 times the IQR from the box edges. In (**c** and **f**), data from three individual transgenic lines with three technical repeats per line are shown. In (**e**), a total of nine biological repeats from three individual *PHR1-WT* lines and a total of eight biological repeats from three individual *PHR1-MUT* lines are shown. Source data are provided as a Source Data file.

m^{6}A loci were confirmed by a SELECT kit (Supplementary Fig. 11a)[85]. This is consistent with the results of single base–resolved m^{6}A profiling, which revealed ~5.6 m^{6}A loci per peak, and the fact that m^{6}A loci tend to form clusters in short regions[24]. This m^{6}A cluster at the 3′ UTR of *PHR1* also appears to be strongly regulated by m^{6}A modification dynamics. The m^{6}A modifications are indeed abolished by mutagenesis in the *PHR1-MUT* transgenic plants (Supplementary Fig. 11b). In addition, the A-to-U mutations did not affect the RNA structure, as demonstrated by the similar minimal free energy of *PHR1-WT* (ΔG = −102.36 kcal/mol) and *PHR1-MUT* (ΔG = −106.66 kcal/mol). Considering the variation in the expression of *PHR1-FLAG-4XMYC* (*PHR1-FM*) in the transgenic plants due to the different copy numbers and insertion sites of the vector, we randomly chose three lines for each transgene for further analysis.

Compared with *PHR1-WT*, the average steady-state level of *PHR1-FM* expression of the three lines was significantly reduced in *PHR1-MUT* plants, but that of the control gene *Basta* was not (Fig. 7c), indicating that m^{6}A enhances the stability of *PHR1* transcripts. Consistent with the expression of *PHR1-FM* (Fig. 7c), transformation with *PHR-WT*, but not *PHR1-MUT*, fully rescued the *phr1* null mutant, which accumulates less

anthocyanin under −P conditions than the WT[49]. Indeed, the *PHR1-MUT* and *phr1* plants exhibited greener leaves than the WT and *PHR1-WT* complementation lines under Pi starvation (Fig. 7d). The average anthocyanin content of the three lines was significantly higher in *PHR1-WT* than in *PHR1-MUT* under −P stress (Fig. 7e and Supplementary Fig. 11c). Furthermore, like the *phr1* null mutant, the average expression levels of two PSI genes downstream of *PHR1* were also significantly reduced in *PHR1-MUT* vs. *PHR1-WT* seedlings (Fig. 7f and Supplementary Fig. 11d). Finally, we carried out target-specific RNA half-life measurements using RT-qPCR to test the role of m^{6}A in the stability of *PHR1* mRNA. The RNA half-life of *PHR1-FM* was significantly reduced in *PHR1-MUT* compared to *PHR1-WT* under both +P and −P conditions (Fig. 7g and Supplementary Fig. 11e). The similar RNA decay pattern of the control gene was indicative of successful cordycepin treatment of both *PHR1-WT* and *PHR1-MUT* materials (Supplementary Fig. 11f). Taken together, these results provide evidence that m^{6}A enhances the stability of *PHR1* transcripts to facilitate PSI signaling.

In summary, the results of physiological and molecular analyses of m^{6}A-mutated transgenic plants demonstrate that m^{6}A enhances the stability of *PHR1* transcripts to facilitate PSI signaling.

Discussion

There is mounting evidence that widespread m^{6}A modifications play critical roles in the post-transcriptional regulation of RNA metabolism and physiological processes[1–3]. Plants are frequently exposed to nutrient-deficient stress, leading to widespread changes in gene expression[39,40]. However, the regulatory function of m^{6}A in responses to these physiological stresses remains elusive. In this study, we examined the m^{6}A-methylome, the transcriptome, genome-wide RNA decay, global profiling of APA sites, PHR1-MTA/MTB protein interactions, and the effects of mutating m^{6}A loci to dissect the role of m^{6}A-mediated regulation of RNA stability in facilitating systemic PSR signaling and Pi homeostasis under Pi-deficient stress. We demonstrated that PHR-mediated PSI-m^{6}A modifications not only promote stability of some PSD transcripts, but also stabilize *PHR1* mRNA to facilitate the expression of PSI genes via a feedback loop (Fig. 7h).

PHR1 and its family members are central TFs in the transcriptional regulation of the PSR[49,53]. Here, we showed that PHRs mediate epitranscriptomic regulation during Pi homeostasis and the PSR. We conducted m^{6}A-seq with systematic calibration using synthetic modification-free RNA libraries to remove false-positive peaks and obtained high-confidence m^{6}A landscapes under normal and Pi-deficient stress conditions (Fig. 1). Pi starvation induced widespread m^{6}A modifications, many of which were added to Pi homeostasis- and PSR-related transcripts (Fig. 2). We also showed that PHR proteins mediate PSI-m^{6}A, as these global modifications were diminished in the *phr1 phl1* double mutant under −P conditions (Fig. 3). However, the PHRs do not transcriptionally regulate the expression of either the PSI-m^{6}A-marked mRNAs or the known m^{6}A methyltransferases or demethylases (Supplementary Fig. 4), raising the interesting question of how PHRs mediate PSI-m^{6}A modifications. Blue light induces the liquid–liquid phase separation of CRYPTOCHROME2 (CRY2) to co-condense the m^{6}A writer proteins MTA, MTB, and FIP37, thereby promoting the addition of m^{6}A to transcripts of the central circadian clock oscillator genes[76]. CRY2 also co-condenses another m^{6}A writer protein, FIO1, to promote the methylation of transcripts encoding multiple regulators of chlorophyll homeostasis[77]. In addition, the histone modification H3K36me3 can guide co-transcriptional m^{6}A modifications in mammals by interacting with METTL14[86]. Analogously, H3K36me2 is highly correlated with m^{6}A modifications in Arabidopsis[87]. Although a limitation exists in that the interaction between PHR1 and MTA/MTB in plants under +P conditions remains uninvestigated, we observed that PHR1 interacts with MTA and MTB in nuclei under −P conditions (Fig. 4). It is plausible that PHRs might act as "m^{6}A recruiters" to guide m^{6}A writers to certain transcripts, facilitating PSR-related m^{6}A methylation upon Pi starvation. These findings expand our understanding of the regulatory functions of PHRs beyond the transcriptional level to the epitranscriptional level.

The m^{6}A modifications regulate almost all aspects of mRNA metabolism, including transcription, pre-mRNA processing, folding, translation, and decay[1–3]. To date, the best-characterized role of m^{6}A in various plant species is its influence on mRNA stability, which affects multiple developmental processes and stress responses[2,3,88]. m^{6}A exerts positive or negative effects on specific transcripts under certain distinct conditions[3,88]. In some studies, the combination of m^{6}A-seq and RNA-seq led to apparently paradoxical conclusions about the effect of m^{6}A on RNA abundance[3,27,36,89]; however, these studies did not directly and globally investigate the relationship between mRNA half-life and m^{6}A modifications in plants. We performed transcriptome-wide RNA decay assays in the WT and a line in which the m^{6}A-writer gene *MTA* is suppressed (*amiR-mta*) under normal and Pi-deficient stress conditions (Fig. 6 and Supplementary Fig. 7). Intriguingly, our results exhibited a distinct effect of m^{6}A modifications on overall mRNA stability, in which m^{6}A mainly destabilizes transcripts under normal growth conditions but stabilizes them under Pi-deficient conditions (Fig. 6 and Supplementary Fig. 7). Our results confirm the dual effects of m^{6}A on mRNA stability, indicating that m^{6}A-mediated RNA decay is dependent on the environment, as exemplified by +P and −P conditions.

We showed that PSI-m^{6}A modifications mediate the regulation of RNA stability in response to Pi starvation. The effects of PSR were previously not well understood at the RNA level; however, our genome-wide RNA decay assay revealed the previously uncharacterized regulation of RNA stability under Pi-deficient stress, in which the half-lives of more than half of transcripts are altered by Pi starvation (Fig. 6c). Approximately 2000 PSD genes show decreased expression levels under Pi starvation (Supplementary Fig. 2e)[53], but it is unclear how this is regulated. Our results show that PHR-controlled PSI-m^{6}A fine-tunes the expression of these PSD genes by stabilizing their transcripts (Figs. 5 and 6). Moreover, we demonstrated that m^{6}A modifications stabilize *PHR1* mRNA to facilitate PSI signaling (Fig. 7). Although the steady-state level of *PHR1* transcript is comparable or moderately increased by −P[49], the mechanism by which its expression is maintained had been unknown. Our findings provide evidence for the post-transcriptional stabilization of *PHR1* mRNA by m^{6}A upon Pi starvation, promoting the downstream signaling pathway.

The above results raise an interesting question about the mechanism of PSI-m^{6}A-mediated RNA decay under −P conditions. m^{6}A reader proteins bind to the m^{6}A modification and determine the fate of m^{6}A-methylated transcripts in diverse RNA metabolic pathways. In mammals, the binding of the m^{6}A reader YTHDF2 to m^{6}A-modified transcripts promotes their decay[90,91], while the binding of other m^{6}A readers (IGF2BP proteins) stabilizes m^{6}A-modified transcripts[92]. In Arabidopsis, the m^{6}A reader EVOLUTIONARILY CONSERVED C-TERMINAL REGION2 (ECT2) binds to and promotes the stability of transcripts related to trichome morphogenesis[93]. The m^{6}A reader CPSF30-L regulate the alternative polyadenylation of some nitrate signaling–related gene transcripts[84]. First, our PAS-seq 2 data showed that the impact of PSI-m^{6}A did not occur through APA shifts (Supplementary Fig. 9). Second, we did not find that *PHR1* was the target of ECT2 in published FA-CLIP-seq data[93]. In addition, a preprint manuscript indicates that the abundance of the m^{6}A reader ECT4 is reduced under Pi-deficiency stress[94]. We further detected the phenotype of *ect2/3/4* under −P stress. Consist with a recent study[95], the primary root length was reduced in *ect2/3/4* compared with the WT under −P treatment (Supplementary Fig. 12a, b). However, the fresh weight and Pi concentration in shoots were comparable between the WT and *ect2/3/4* under −P conditions (Supplementary Fig. 12c, d). As expected, *PHR1* expression and mRNA stability were unchanged in *ect2/3/4* versus the WT under −P conditions (Supplementary Fig. 12e, f). These results

indicated that m^{6}A readers ECT2/3/4 do not participate in PSI-m^{6}A-mediated *PHR1* stabilization.

Our results suggest that unknown PSR m^{6}A reader(s) modulate PSI-m^{6}A-mediated mRNA stabilization. It would therefore be interesting to systematically investigate the activities of m^{6}A readers upon Pi starvation.

In conclusion, we analyzed the m^{6}A-methylome, transcriptome, PHR1-MTA/MTB protein interactions, global APA site profiling, and mRNA decay landscape (validated by m^{6}A-loci mutagenesis) to systematically investigate the role of the m^{6}A modification in the PSR. Our findings demonstrate that PHR-mediated stress-induced m^{6}A modifications play a crucial role in maintaining Pi homeostasis and enhancing systemic PSR signaling by stabilizing PSR-related transcripts. These findings uncover how plants respond to nutrition-deficient stress at the epitranscriptome level.

Methods

Plant materials and growth conditions

Seeds of Arabidopsis (*Arabidopsis thaliana*) accession Columbia (Col-0) and the *phr1* (SALK_067629C), *phl1* (CS832612), and *ect2/3/4* (CS2110132) T-DNA null mutants were obtained from the Arabidopsis Biological Resource Center (https://abrc.osu.edu/). The *phr1 phl1* double mutant was obtained by crossing *phr1* with the *phl1* single mutant. To generate *amiR-mta* plants, Col-0 plants were transformed with the binary vector pBA-P_{35S}:amiR-mta by the floral dip method[96]. Similarly, for *P_{PHR1}:gPHR1-FLAG-4XMYC-3UTR-WT; phr1* and *P_{PHR1}:gPHR1-FLAG-4XMYC-3UTR-MUT; phr1* plants, homozygous *phr1* mutants were transformed with the binary vectors pBA002a-P_{PHR1}:gPHR1-FLAG-4XMYC-3UTR-WT or pBA002a-P_{PHR1}:gPHR1-FLAG-4XMYC-3UTR-MUT by the floral dip method[96].

The wild type (Col-0), mutants, and transgenic lines were grown under a 12-h-light/12-h-dark photoperiod at 22 °C at a relative humidity of ~50%. For Pi starvation treatment, seeds were germinated and grown on Murashige and Skoog (MS) agar medium supplemented with 1% sucrose for seven days. The seven-day-old plants were transferred from MS agar medium to fresh MS agar medium containing 1.25 mM Pi (+P) or 6.25 μM Pi (−P) and incubated for seven more days.

Vector construction

Most coding and genomic sequences were cloned into the pENTR/D-TOPO (ThermoFisher) vector and confirmed by Sanger sequencing. Most plant constructs were generated using the Gateway cloning system (ThermoFisher). The primers for all constructs are listed in Supplementary Data 5.

The pBA-P_{35S}:amiR-mta plasmid was constructed as follows: First, the sequence of artificial miRNA used to silence *MTA* (*amiR-mta*) was designed using the WMD3 website (http://wmd3.weigelworld.org)[97]. The *amiR-mta* sequence was introduced into a pENTER vector containing the primary-miR159a (pri-miR159a) stem-loop sequence by PCR to obtain pENTR-pri-amiR-mta-159a. Finally, *pri-amiR-mta-159a* was transferred into pBA-P_{35S}:DC to yield pBA-P_{35S}:amiR-mta.

pBA002a-P_{PHR1}:gPHR1-FLAG-4XMYC-3UTR-WT and pBA002a-P_{PHR1}: gPHR1-FLAG-4XMYC-3UTR-MUT were constructed as follows: First, an approximately 2.4 kb promoter and 5′ UTR fragment of *PHR1* was amplified from the Col-0 genome and cloned into AscI/XbaI-digested pBA002a-DC-FLAG-4XMYC (FM) to generate pBA002a-P_{PHR1}:DC-FM vector using MultiF Seamless Assembly Mix (ABclonal). The *PHR1* genomic fragment without the stop codon was amplified from the Col-0 genome and cloned into the pENTR/D vector to create the pENTR-gPHR1 vector. gPHR1 was transferred into pBA002a-P_{PHR1}:DC-FM to yield the pBA002a-P_{PHR1}:gPHR1-FM vector. Finally, a 663 bp fragment of wild-type *PHR1* after the stop codon was amplified from the Col-0 genome and cloned into the SacI-digested pBA002a-P_{PHR1}:gPHR1-FM vector using MultiF Seamless Assembly Mix (ABclonal) to yield pBA002a-P_{PHR1}:gPHR1-FLAG-4XMYC-3UTR-WT. The corresponding 3′ UTR of *PHR1* with the m^{6}A-loci mutated was synthesized and cloned into the SacI-digested pBA002a-P_{PHR1}:gPHR1-FM vector using MultiF Seamless Assembly Mix (ABclonal) to yield pBA002a-P_{PHR1}:gPHR1-FLAG-4XMYC-3UTR-MUT.

Y2H vectors were constructed as follows: full-length CDSs of *PHR1*, *MTA*, *MTB*, *FIP37*, *SPX1*, and *SPX2* were amplified and cloned into the NotI/AscI-digested pENTR/D-TOPO vector using MultiF Seamless Assembly Mix (ABclonal) and confirmed by sequencing. The CDSs were inserted into pGADT7-GW and pGBKT7-GW vectors to generate AD-gene and BD-gene vectors by LR reaction, respectively.

The PHR1-YN BiFC vector was constructed as follows: the full-length CDS of *PHR1* was amplified and cloned into SalI/SpeI-digested pCAMBIA-35S-nYFP vector to generate pCAMBIA-35S-PHR1-nYFP (PHR1-YN) using MultiF Seamless Assembly Mix (ABclonal).

Synthesis of modification-free IVT RNA

Modification-free IVT RNA was synthesized as previously described[22]. The oligonucleotides were synthesized at Genscript and are listed in Supplementary Data 5.

Total RNA was extracted from the corresponding Pi starvation-treated or control samples using TRIzol (ThermoFisher). Cellular mRNA was isolated from the samples using Dynabeads Oligo(dT)$_{25}$ (ThermoFisher) according to the manufacturer's instructions. For first-strand cDNA synthesis, 100 ng of mRNA was hybridized with 1 μl of poly(T) primer (12 μM) at 75 °C for 3 min and 42 °C for 2 min. Subsequently, a mixture containing 2 μl of 5× first-strand buffer for SMARTScribe Reverse Transcriptase (Takara), 0.5 μl of 100 mM DTT, 0.5 μl of SUPERase-In RNase Inhibitor (ThermoFisher), 1 μl of TSO T7 primer (10 μM), 1 μl of 50× Advantage UltraPure PCR Deoxynucleotide Mix (Takara), and 1 μl of SMARTScribe Reverse Transcriptase (Takara) was added to the mRNA–poly(T) primer mixture. The reaction was incubated at 42 °C for 1.5 h and stopped by heating at 68 °C for 10 min.

For double-stranded cDNA synthesis, following the addition of 10 μl of 10× Advantage 2 PCR buffer (Takara), 1 μl of Advantage 2 PCR Polymerase Mix (Takara), 2 μl of 50× Advantage UltraPure PCR Deoxynucleotide Mix (Takara), 2 μl of T7 extension primer (10 μM), 2 μl of RNase H (NEB), and RNase-free water to a final volume of 100 μl, the primer extension reaction was conducted at 37 °C for 15 min, 95 °C for 2 min, 60 °C for 1 min, and 68 °C for 10 min. Double-stranded cDNA was purified using the AMPure XP beads (Beckman).

For T7 RNA polymerase-mediated transcription, in vitro transcription was performed at 37 °C for 2 h using a HiScribe T7 High Yield RNA Synthesis kit (NEB) with modification-free NTPs from Takara Bio (Cat# 6140). The reaction mixture was treated with TURBO DNase (ThermoFisher) at 37 °C for 30 min to remove the dsDNA and was purified using RNAClean XP beads (Beckman).

LC-MS/MS quantification of m^{6}A

To quantify the contents of m^{6}A RNA modifications in cellular mRNA from WT, *amiR-mta* plants, and IVT RNA, 100 ng of cellular mRNA or IVT RNA was digested with 1U Nuclease P1 (NEB) at 37 °C for 4 h, followed by the addition of 1U Shrimp Alkaline Phosphatase (NEB) and 100 mM MES (pH 6.5) and incubation at 37 °C for 4 h. The digested samples were centrifuged at 15,000 × *g* for 5 min, and the supernatants were subjected to LC-MS/MS analysis at the Institute of Botany, Chinese Academy of Sciences. The detailed method used for the LC-MS/MS analysis was described previously[36].

m^{6}A-seq

m^{6}A-seq was performed as previously described[98]. In brief, approximately 50 μg of total RNA was extracted from Pi starvation-treated or untreated 14-day-old WT and *phr1 phl1* seedlings using TRIzol reagent (ThermoFisher). Cellular mRNA was isolated from the samples using Dynabeads Oligo(dT)$_{25}$ (ThermoFisher) according to the manufacturer's instructions. The cellular mRNA or IVT RNA was fragmented

to approximately 100 nucleotide (nt) segments with a Magnesium RNA fragmentation module (NEB) and purified by ethanol precipitation. Ten percent of the fragmented RNA was kept as input. The concentration of the fragmented RNA was measured by Qubit (ThermoFisher).

m^{6}A immunoprecipitation (IP) was performed using commercial anti-m^{6}A antibody from NEB (Cat# E1610S). Fragmented RNA (200 ng) was incubated with 1 μl of anti-m^{6}A antibody in 200 μl of IP buffer (10 mM Tris-HCl pH 7.5, 150 mM NaCl, 0.1% v/v Igepal [CA-6300] and 0.2 U/μl SUPERase-In RNase Inhibitor [ThermoFisher] in nuclease-free water) at 4 °C for 2 h on an orbital rotator. After adding 25 μl of Dynabeads Protein G magnetic beads (ThermoFisher), the m^{6}A-IP mixtures were incubated at 4 °C for 2 h. The beads were washed twice successively with low-salt buffer (50 mM NaCl, 10 mM Tris-HCl pH 7.5, 0.1% Igepal CA-630 in nuclease-free water) and high-salt buffer (500 mM NaCl, 10 mM Tris-HCl pH 7.5, 0.1% Igepal CA-630 in nuclease-free water).

RNA eluted from the beads and non-IP fragments (input control) were used to prepare libraries with a Stranded mRNA-seq Lib Prep Module for Illumina (ABclonal). The libraries of two biological repeats for each sample were sequenced as 150-bp paired-end reads on a NovaSeq 6000 instrument at Novogene.

m^{6}A-seq data analysis

Approximately 23 million paired-end 150 bp (PE150) reads were obtained for each sample. Raw reads were subjected to adapter trimming and filtering of low-quality reads (quality <20) using Cutadapt (v4.1) software[99]. Basic quality control was conducted using FastQC (v0.11.9) (www.bioinformatics.babraham.ac.uk/projects/fastqc/), and reads <15 bp long were discarded. Quality-filtered reads were mapped to the Arabidopsis genome (TAIR10) using HISTA2 (v2.2.1)[100] with the parameter '–rna-strandness RF'. Mapped reads were visualized in Integrative Genomics Viewer (IGV)[101] after RPKM (Reads Per Kilobase per Million mapped reads) normalization and used for the following analyses.

First, m^{6}A peaks were called using the R package exomePeak (v2.16.0) (bioconductor.org/packages//2.13/bioc/html/exomePeak.html) using the enrichment criteria (IP/Input) ≥ 2 and FDR < 0.05. Systematic calibration using modification-free IVT RNA libraries was then performed as previously described[22]. Briefly, false-positive peaks were defined as the overlapping/common peaks sharing more than 50% fractions of peak regions in the endogenous mRNA library and modification-free IVT RNA library. BEDtools (v2.30.0) intersect[102] was used to find the overlapping peaks. The calibrated high-confidence m^{6}A peaks were defined as peaks that were specifically identified in both biological replicates in mRNA m^{6}A-seq libraries but not in IVT RNA m^{6}A libraries. The differential m^{6}A peaks were then identified using exomePeak based on the criteria of fold-change ≥ 1.5 and FDR < 0.05. The differential m^{6}A peaks that overlapped with known false-positive m^{6}A peaks were removed. Peak annotation was performed using BEDtools (v2.30.0)[102]. HOMER (v4.11) software (homer.ucsd.edu/homer/motif) was used to identify m^{6}A peak motifs in the calibrated high-confident m^{6}A peaks and peak motifs in peaks from the IVT RNA libraries.

RNA-seq data analysis

The non-m^{6}A-IP control/Input RNA-seq data were used for transcriptome analysis of WT and *phr1 phl1* plants under +P and −P conditions. The RNA-seq data from the RNA decay assay at 0 min were used for transcriptome analysis of WT and *amiR-mta* plants. Approximately 21 to 34 million paired-end 150 bp (PE150) reads were obtained for each sample.

Raw reads were subjected to adapter trimming and filtering of low-quality reads (quality <20) using Cutadapt (v4.1) software[99]. Basic quality control was conducted using FastQC (v0.11.9) (www.bioinformatics.babraham.ac.uk/projects/fastqc/). Filtered reads were mapped to the Arabidopsis genome (TAIR10) using HISTA2 (v2.2.1)[100]. Only uniquely mapped reads were retained for read counting and differential gene expression analysis. The read counts for each gene were calculated using featureCounts[103] and normalized using DESeq2 (v1.38)[104]. The differentially expressed genes were identified using DESeq2 (v1.38)[104].

Y2H assay

Y2H assay was performed as previously described[105]. The Matchmaker Gold Y2H system (Clontech) was used. Different combinations of constructs were co-transformed into the Y2H Gold yeast strain (Clontech) and grown on synthetic defined medium plates under a screening condition. For each combination, a minimum of ten independent colonies were subjected to interaction testing. The corresponding colonies were picked up and spotted onto the selective plates in 1:10 serial dilutions for picture recording.

Bimolecular fluorescence complementation assay (BiFC) and fluorescence microscopy

The BiFC experiments were performed as previously described[75]. All BiFC constructs were transformed into *Agrobacterium tumefaciens* strain GV3101. The resulting positive Agrobacterium colonies harboring each construct were cultured in Luria-Bertani medium containing 100 μg/mL kanamycin and 40 μM acetosyringone at 28 °C to an optical density at 600 nm (OD_{600}) = 1.0. Then, the Agrobacterium cells were resuspended with the infiltration buffer (10 mM $MgCl_2$ and 150 μM acetosyringone) and incubated at room temperature for 3 h without shaking. Next, equal volumes of the corresponding Agrobacterium cell suspensions were mixed and co-infiltrated into the leaves of 4-week-old *N. benthamiana*. The fluorescence signals (YFP emission at 514 nm) were observed at 48 h after infiltration with a Zeiss LSM900 confocal laser scanning microscope.

Nuclei isolation

Nuclei isolation was performed as described previously[74]. In brief, ~1 g of ground powder was dissolved in 4 ml lysis buffer (20 mM Tris-HCl pH 7.5, 20 mM KCl, 2.5 mM $MgCl_2$, 25% [v/v] glycerol, 250 mM sucrose, 5 mM DTT, and 1× proteinase inhibitor cocktail without EDTA [Roche]). The homogenate was filtered through a double layer of Miracloth. The flow-through was centrifuged at 1500 × *g* for 10 min at 4 °C. After discarding the supernatant, the pellet was washed three times with 5 ml nuclear resuspension buffer (20 mM Tris-HCl pH 7.5, 2.5 mM $MgCl_2$, 25% [v/v] glycerol, and 0.2% [v/v] Triton X-100). The pellet was resuspended in 500 μl of nuclear resuspension buffer 2 (20 mM Tris-HCl pH 7.5, 2.5 mM $MgCl_2$, 25% [v/v] glycerol, 250 mM sucrose, 5 mM β-ME, 0.5% [v/v] Triton X-100, and 1× proteinase inhibitor cocktail without EDTA [Roche]) and transferred to 500 μl nuclear resuspension buffer 3 (20 mM Tris-HCl pH 7.5, 10 mM $MgCl_2$, 1.7 M sucrose, 5 mM β-ME, 0.5% [v/v] Triton X-100, and 1× proteinase inhibitor cocktail without EDTA [Roche]). After centrifugation at 10,000 × *g* for 60 min at 4 °C, the isolated nuclei were subjected to immunoblotting or co-immunoprecipitation (Co-IP).

Co-IP

Co-IP was performed as described with some modifications[59,105]. The isolated nuclei of *PHR1-WT* were lysed in 0.9 ml IP buffer (40 mM Tris-HCl pH 7.5, 5 mM $MgCl_2$, 150 mM NaCl, 100 nM $ZnCl_2$, 1 mM DTT, 1% [v/v] Triton X-100, 5% [v/v] glycerol, 1 mM PMSF, 50 μM NaCl, and 1× proteinase inhibitor cocktail without EDTA [Roche]). Then, the lysate was treated with Turbo DNase (ThermoFisher) for 2 h at 4 °C. After centrifugation at 10,000 × *g* for 10 min at 4 °C, the supernatants were transferred to a new 2 ml tube. Five percent of the supernatant served as input, and the remaining was immunoprecipitated with the anti-Myc antibody (Sigma, Cat# C3956) for 2 h at 4 °C. Next, Dynabeads protein

G Magnetic beads (ThermoFisher) were used to pull down the PHR1 complexes. The beads with PHR1 complexes were washed four times with IP buffer before application of SDS loading buffer at 95 °C for 10 min.

Immunoblot analysis

Immunoblot analysis was performed as described[105]. The ground powders of materials, isolated nuclei and immunoprecipitated beads were mixed with SDS loading buffer (80 mM Tris-HCl pH 6.8, 2% SDS, 10% glycerol, 0.1 M DTT, and 0.005% Bromophenol blue) and then incubated at 95 °C for 10 min. Next, the extracted proteins in the supernatant were subjected to immunoblots. The blots were probed with primary antibodies against Myc (Sigma, Cat# C3956, IB 1:3000), MTA (homemade from Z. Zhang's group, IB 1:1000)[74,75], MTB (homemade from Z. Zhang's group, IB 1:1000)[74,75], AGO1 (Agrisera, Cat# AS09 527, IB 1:2000), and Histone H3 (ABclonal, Cat# A17562, IB 1:5000). The secondary antibody was the HRP-conjugated goat anti-rabbit IgG (ThermoFisher, Cat# 31460).

PAS-seq 2 and data analysis

Poly(A) sequencing (PAS-seq) 2 was performed as described previously[83]. In brief, total RNA was extracted from 14-day-old Arabidopsis seedlings using TRIzol™ reagent (ThermoFisher) according to the manufacturer's instructions. Poly(A) RNA was enriched using Dynabeads Oligo$(dT)_{25}$ beads (ThermoFisher). The enriched RNA was fragmented using RNA Fragmentation Reagents (ThermoFisher, AM8740) at 70 °C for 5 min. Next, fragmented mRNAs were subjected to first-strand cDNA synthesis by SuperScript III reverse transcriptase (ThermoFisher) with the PAS-seq 2 oligo(dT) primer (GTGACT GGAGTTCCTTGGCACCCGAGAATTCCATTTTTTTTTTTTTTTTTTTV, where V represents A/C/G) and a template-switch oligo (TSO) containing locked nucleic acid (LNA) (CTACACGACGCTC TTCCGATCTCATrGrG+G). The cDNA was purified with AMPure XP beads (Beckman) and amplified with Illumina TruSeq Universal adapter and RNA PCR indexed primer. Amplified products were gel extracted to isolate fragments of 185–225 bp. Purified fragments were sequenced on an Illumina sequencing platform.

Data analysis was performed as described in previous studies[84]. In brief, raw reads were trimmed to remove adapters and filtered for low-quality bases ($Q < 20$) using Cutadapt (v4.1). The filtered reads were aligned to the *Arabidopsis thaliana* genome (TAIR10) using STAR (v2.7.10). Internal priming artifacts, defined as six or more continuous As or seven or more As in a 10-nt window downstream from the poly(A) junction, were discarded. Next, polyadenylation sites (PASs) located within a 24-nt window and with TPM ≥ 3 in at least two biological replicates were clustered into a PAS cluster (PAC). The PAS shift events between indicated samples were compared with Fisher's exact test. A pair of PAS shifts with FDR < 0.01 was considered significant. For genes with more than two significantly shifted PACs, the two most dominant differential PACs were selected to represent the shift orientation of the given genes.

Gene Ontology (GO) term analysis

GO analysis was performed with TBtools (v2.019)[106].

Transcriptome-wide RNA decay analysis

The analysis of transcriptome-wide RNA decay was performed as described[79] (bioconductor.org/packages/release/bioc/html/RNAdecay.html) with some modifications. Pi starvation-treated (−P) or untreated control (+P) two-week-old Col-0 (WT) and *amiR-mta* seedlings were harvested and placed in incubation buffer containing 15 mM sucrose, 1 mM KCl, 1 mM PIPES pH 6.25, and 1 mM sodium citrate. The transcriptional inhibitor cordycepin was then added to the incubation buffer to a final concentration of 1 mM. Vacuum infiltration (~12 psi) was conducted for 1 min to facilitate sample penetration. Initial (0 min, T_0) samples were immediately harvested and flash-frozen in liquid nitrogen. Then, vacuum infiltration (~12 psi) was performed twice for 1 min each time. Subsequently, samples were collected at 15, 30, 60, and 120 min following the first vacuum release, flash-frozen in liquid nitrogen, and ground to a powder. Three biological replicates were conducted for each time point and each material. Total RNA was extracted from the samples using TRIzol (ThermoFisher) and used to prepare libraries with a Stranded mRNA-seq Lib Prep Module for Illumina (ABclonal). The libraries were sequenced as 150-bp paired-end reads on an NovaSeq 6000 instrument at Annoroad.

The raw sequencing reads from the RNA decay RNA-seq were subjected to adapter trimming and filtering of low-quality reads (quality <20) using Cutadapt (v4.1)[99]. Clean reads were mapped to the Arabidopsis genome (TAIR10) using HISTA2 (v2.2.1)[100]. Only uniquely mapped reads were retained for the following analyses. The featureCounts[103] was used to obtain raw read counts for all annotated genes. PCA was performed with plotPCA from the DESeq2 R package[104]. Normalization and modeling of RNA decay data were carried out using the package 'RNAdecay' (bioconductor.org/packages/release/bioc/html/RNAdecay.html). Specifically, 30 stably and highly expressed genes in WT and *amiR-mta* under +P and −P conditions ("AT1G44575", "AT1G30380", "AT5G42980", "AT5G65220", "AT2G20260", "AT4G01310", "AT2G37660", "AT3G01480", "AT5G08650", "ATCG00800", "AT3G02730", "AT5G59613", "AT5G38520", "AT3G11930", "AT5G41700", "AT5G03880", "AT1G76200", "AT2G44650", "AT2G42210", "AT5G16710", "AT1G02920", "AT4G20150", "AT1G21065", "AT2G21960", "AT1G20850", "AT2G24940", "AT1G66670", "AT1G15120", "AT5G16400", "AT3G12260") were chosen for data normalization. ComplexHeatmap[107] was employed to draw the RNA decay heatmap, which was constructed using the mean relative abundance and half-life of each transcript (Supplementary Data 3).

Measurement of target-specific RNA decay

Cordycepin treatment was performed as described above (for the transcriptome-wide RNA decay assay). Seedlings were collected at 0 min, 1 h, and 4 h following the first vacuum release, frozen in liquid nitrogen, and ground to a powder. Total RNA was extracted from the samples for reverse transcription and quantification of the expression levels of various genes by quantitative reverse-transcription PCR. *EF1α* (AT1G07940) was used as an internal control. All primers used are listed in Supplementary Data 5.

Validation of m^{6}A sites in target mRNAs

The *PHR1* m^{6}A sites were validated using the SELECT kit (EPIBIOTECH, Cat. No: R202106M-0224T)[85]. Briefly, 1 μg total RNA of each sample was equally divided into two fractions: one was treated with the m^{6}A demethylase FTO at 37 °C for 30 min, and the other was treated with FTO and EDTA under the same conditions. Probes were designed to target the region flanking the tested m^{6}A sites for annealing and extension. The extended products were ligated using SELECT™ ligase, followed by qPCR to validate the m^{6}A modification. The probes and primers used are listed in Supplementary Data 5.

Gene-specific m^{6}A-IP-qPCR

The gene-specific m^{6}A-IP-qPCR was performed as described in a previous study[19]. In brief, approximately 200 ng isolated mRNAs was fragmented to 100–150 nt using the Magnesium RNA Fragmentation Module (NEB) and purified by ethanol precipitation. The commercial m^{6}A probes (NEB, Cat# E1610S) and non-m^{6}A probes (NEB, Cat# E1610S) were mixed into the eluted fragmented RNAs as positive and negative controls, respectively. Ten percent of the RNA mixture served as input sample, and the remaining was incubated with 1 μl anti-m^{6}A antibody (NEB, Cat# E1610S) in 200 μl of IP buffer (10 mM Tris-HCl pH 7.5, 150 mM NaCl, 0.1% v/v Igepal [CA-6300], and 0.2 U/μl SUPERase-In

RNase Inhibitor [ThermoFisher] in nuclease-free water) at 4 °C for 2 h on an orbital rotator. The m^{6}A-containing RNA fragments were pulled down and eluted according to the above m^{6}A-seq procedure. Both input and IP samples were analyzed by RT-qPCR using primers listed in Supplementary Data 5. The enrichment of m^{6}A in each sample was calculated by normalizing the value of the amplification cycle (Cq) of the IP to that of the corresponding input. The relative enrichment of each m^{6}A region in samples was normalized to that of *PHR1-WT*, where the ratio was arbitrarily set to 1.

Quantitative reverse-transcription PCR

Total RNA was extracted from two-week-old Pi starvation-treated seedlings using TRIzol reagent (ThermoFisher). RNA quality was checked by formaldehyde gel electrophoresis. The total RNA was treated with TURBO DNase (ThermoFisher), and 1 μg of DNase-treated RNA was subjected to reverse transcription with SuperScript II. Quantitative real-time PCR (qPCR) was performed using SYBR Green Master Mix (ThermoFisher). The $2^{-\Delta\Delta CT}$ method was used to calculate gene expression levels. *EF1α* (AT1G07940) was used as an internal control. All primers used are listed in Supplementary Data 5.

Measuring phosphate (Pi) content

Measurements of Pi concentrations in plants were carried out as previously described[50]. In brief, 10–20 mg of fresh plant samples were placed in 1.5 ml Eppendorf tubes, frozen in liquid nitrogen, and ground to a powder using a Tissuelyser-24 (JINGXIN). After adding 500 μl of 1% acetic acid, the sample was incubated in the dark at 4 °C for 30 min with a shaking at 15 min. The mixture was centrifuged at 4 °C, 12,000 × *g* for 10 min, and 90 μl of the supernatant was transferred to a new 1.5 ml Eppendorf tube. The sample was mixed with 210 μl of reaction buffer containing 0.42% ammonium molybdate and 10% ascorbic acid (v/v, 6:1). The sample was incubated at 37 °C for 1 h, and the optical density (OD) at 820 nm was measured in a Spark Multimode Microplate Reader (Tecan). A standard curve was constructed using different concentrations of KH_2PO_4 (0, 0.5, 1, 2.5, 5, 7.5, 10, 15, 25, 30, 50 nmol), and the Pi concentrations in shoots were calculated.

Measuring anthocyanin content

Anthocyanin content was measured as previously described[53]. After measuring the fresh weight of each sample (typically 0.1–0.5 g), the sample was treated with 1 ml of anthocyanin extraction buffer composed of propanol/HCl/H_2O at a ratio of 18/1/81 (v/v/v). Following overnight incubation at room temperature in the dark, the samples were centrifuged at 12,000 × *g* for 20 min. The supernatants were diluted two-fold with extraction buffer, and their absorbance (A) was measured at 535 nm and 650 nm. The relative anthocyanin content was then determined using the formula: 2× (A_{535}−A_{650}) per gram of fresh weight.

Statistics and reproducibility

Primary root lengths were measured with ImageJ (https://imagej.net/software/fiji/). Details of statistical analysis, including the statistical tests used, exact *n* values for each measurement, and *P* values, are presented in the figure legends and figures. All experiments were independently repeated at least once and showed similar results. No statistical method was used to predetermine sample size. No data were excluded from the analyses.

Reporting summary

Further information on research design is available in the Nature Portfolio Reporting Summary linked to this article.

Data availability

All data are available in the main text or the supplementary materials. The raw sequencing data of m^{6}A-seq, RNA-seq, transcriptome-wide RNA decay assay, and PAS-seq 2 generated in this study have been deposited in the Genome Sequence Archive (GSA) under accession code CRA016391. The processed results of m^{6}A-seq, RNA-seq, transcriptome-wide RNA decay assay, and PAS-seq 2 are available in Supplementary Datas 1–4. Source Data are provided with this paper. Plasmids and transgenic plants generated in this study will be available from the corresponding author upon request. Source data are provided with this paper.

References

1. Zhao, B. S., Roundtree, I. A. & He, C. Post-transcriptional gene regulation by mRNA modifications. *Nat. Rev. Mol. Cell Biol.* **18**, 31–42 (2017).
2. Shen, L., Ma, J., Li, P., Wu, Y. & Yu, H. Recent advances in the plant epitranscriptome. *Genome Biol.* **24**, 43 (2023).
3. Tang, J., Chen, S. & Jia, G. Detection, regulation, and functions of RNA N(6)-methyladenosine modification in plants. *Plant Commun.* **4**, 100546 (2023).
4. Zaccara, S., Ries, R. J. & Jaffrey, S. R. Reading, writing and erasing mRNA methylation. *Nat. Rev. Mol. Cell Biol.* **20**, 608–624 (2019).
5. Sharma, B., Prall, W., Bhatia, G. & Gregory, B. D. The diversity and functions of plant RNA modifications: what we know and where we go from here. *Annu. Rev. Plant Biol.* **74**, 53–85 (2023).
6. Liu, J. et al. A METTL3-METTL14 complex mediates mammalian nuclear RNA N6-adenosine methylation. *Nat. Chem. Biol.* **10**, 93–95 (2014).
7. Jia, G. et al. N6-methyladenosine in nuclear RNA is a major substrate of the obesity-associated FTO. *Nat. Chem. Biol.* **7**, 885–887 (2011).
8. Zheng, G. et al. ALKBH5 is a mammalian RNA demethylase that impacts RNA metabolism and mouse fertility. *Mol. Cell* **49**, 18–29 (2013).
9. Zhong, S. et al. MTA is an Arabidopsis messenger RNA adenosine methylase and interacts with a homolog of a sex-specific splicing factor. *Plant Cell* **20**, 1278–1288 (2008).
10. Shen, L. et al. N(6)-methyladenosine RNA modification regulates shoot stem cell fate in Arabidopsis. *Dev. Cell* **38**, 186–200 (2016).
11. Růžička, K. et al. Identification of factors required for m(6) A mRNA methylation in Arabidopsis reveals a role for the conserved E3 ubiquitin ligase HAKAI. *New Phytol.* **215**, 157–172 (2017).
12. Wong, C. E. et al. Shaping the landscape of N6-methyladenosine RNA methylation in Arabidopsis. *Plant Physiol.* **191**, 2045–2063 (2023).
13. Shen, L. Functional interdependence of N6-methyladenosine methyltransferase complex subunits in Arabidopsis. *Plant Cell* **35**, 1901–1916 (2023).
14. Xu, T. et al. FIONA1-mediated m(6) a modification regulates the floral transition in Arabidopsis. *Adv. Sci.* **9**, e2103628 (2022).
15. Wang, C. et al. FIONA1 is an RNA N(6)-methyladenosine methyltransferase affecting Arabidopsis photomorphogenesis and flowering. *Genome Biol.* **23**, 40 (2022).
16. Sun, B. et al. FIONA1-mediated methylation of the 3′UTR of FLC affects FLC transcript levels and flowering in Arabidopsis. *PLoS Genet.* **18**, e1010386 (2022).
17. Duan, H. C. et al. ALKBH10B is an RNA N(6)-methyladenosine demethylase affecting Arabidopsis floral transition. *Plant Cell* **29**, 2995–3011 (2017).
18. Martínez-Pérez, M. et al. Arabidopsis m(6)A demethylase activity modulates viral infection of a plant virus and the m(6)A abundance in its genomic RNAs. *Proc. Natl. Acad. Sci. USA* **114**, 10755–10760 (2017).
19. Tang, J. et al. The RNA N(6) -methyladenosine demethylase ALKBH9B modulates ABA responses in Arabidopsis. *J. Integr. Plant Biol.* **64**, 2361–2373 (2022).

20. Meyer, K. D. DART-seq: an antibody-free method for global m(6)A detection. *Nat. Methods* **16**, 1275–1280 (2019).
21. Helm, M., Lyko, F. & Motorin, Y. Limited antibody specificity compromises epitranscriptomic analyses. *Nat. Commun.* **10**, 5669 (2019).
22. Zhang, Z. et al. Systematic calibration of epitranscriptomic maps using a synthetic modification-free RNA library. *Nat. Methods* **18**, 1213–1222 (2021).
23. Baquero-Pérez, B. et al. N6-methyladenosine modification is not a general trait of viral RNA genomes. *Nat. Commun.* **15**, 1964 (2024).
24. Liu, C. et al. Absolute quantification of single-base m(6)A methylation in the mammalian transcriptome using GLORI. *Nat. Biotechnol.* **41**, 355–366 (2023).
25. Yue, H., Nie, X., Yan, Z. & Weining, S. N6-methyladenosine regulatory machinery in plants: composition, function and evolution. *Plant Biotechnol. J.* **17**, 1194–1208 (2019).
26. Hu, J. et al. N(6) -Methyladenosine mRNA methylation is important for salt stress tolerance in Arabidopsis. *Plant J.* **106**, 1759–1775 (2021).
27. Anderson, S. J. et al. N(6)-methyladenosine inhibits local ribonucleolytic cleavage to stabilize mRNAs in Arabidopsis. *Cell Rep.* **25**, 1146–1157.e1143 (2018).
28. Gao, Y. et al. Drought induces epitranscriptome and proteome changes in stem-differentiating xylem of Populus trichocarpa. *Plant Physiol.* **190**, 459–479 (2022).
29. Hou, N. et al. MdMTA-mediated m(6) A modification enhances drought tolerance by promoting mRNA stability and translation efficiency of genes involved in lignin deposition and oxidative stress. *New Phytol.* **234**, 1294–1314 (2022).
30. Liu, G., Wang, J. & Hou, X. Transcriptome-wide N(6)-methyladenosine (m(6)A) methylome profiling of heat stress in pak-choi (Brassica rapa ssp. chinensis). *Plants (Basel)* **9**, 1080 (2020).
31. Govindan, G. et al. mRNA N(6) -methyladenosine is critical for cold tolerance in Arabidopsis. *Plant J.* **111**, 1052–1068 (2022).
32. Zhang, M. et al. N(6)-methyladenosine RNA modification regulates photosynthesis during photodamage in plants. *Nat. Commun.* **13**, 7441 (2022).
33. Zhang, K. et al. The dynamics of N(6)-methyladenine RNA modification in interactions between rice and plant viruses. *Genome Biol.* **22**, 189 (2021).
34. Zhang, T. et al. N6-methyladenosine RNA modification promotes viral genomic RNA stability and infection. *Nat. Commun.* **13**, 6576 (2022).
35. Guo, T. et al. The m(6) A reader MhYTP2 regulates MdMLO19 mRNA stability and antioxidant genes translation efficiency conferring powdery mildew resistance in apple. *Plant Biotechnol. J.* **20**, 511–525 (2022).
36. Zhou, L., Tian, S. & Qin, G. RNA methylomes reveal the m(6)A-mediated regulation of DNA demethylase gene SlDML2 in tomato fruit ripening. *Genome Biol.* **20**, 156 (2019).
37. Cheng, P. et al. RNA N(6)-methyladenosine modification promotes auxin biosynthesis required for male meiosis in rice. *Dev. Cell* **57**, 246–259.e244 (2022).
38. Zhou, L. et al. N(6)-methyladenosine RNA modification regulates strawberry fruit ripening in an ABA-dependent manner. *Genome Biol.* **22**, 168 (2021).
39. Schachtman, D. P. & Shin, R. Nutrient sensing and signaling: NPKS. *Annu. Rev. Plant Biol.* **58**, 47–69 (2007).
40. Bailey-Serres, J., Parker, J. E., Ainsworth, E. A., Oldroyd, G. E. D. & Schroeder, J. I. Genetic strategies for improving crop yields. *Nature* **575**, 109–118 (2019).
41. Qi, W., Baldwin, S. A., Muench, S. P. & Baker, A. Pi sensing and signalling: from prokaryotic to eukaryotic cells. *Biochem. Soc. Trans.* **44**, 766–773 (2016).
42. Wild, R. et al. Control of eukaryotic phosphate homeostasis by inositol polyphosphate sensor domains. *Science* **352**, 986–990 (2016).
43. Xu, C. et al. A phosphate-sensing organelle regulates phosphate and tissue homeostasis. *Nature* **617**, 798–806 (2023).
44. Lambers, H. Phosphorus acquisition and utilization in plants. *Annu. Rev. Plant Biol.* **73**, 17–42 (2022).
45. López-Arredondo, D. L., Leyva-González, M. A., González-Morales, S. I., López-Bucio, J. & Herrera-Estrella, L. Phosphate nutrition: improving low-phosphate tolerance in crops. *Annu. Rev. Plant Biol.* **65**, 95–123 (2014).
46. Cong, W. F., Suriyagoda, L. D. B. & Lambers, H. Tightening the phosphorus cycle through phosphorus-efficient crop genotypes. *Trends Plant Sci.* **25**, 967–975 (2020).
47. Paz-Ares, J. et al. Plant adaptation to low phosphorus availability: core signaling, crosstalks, and applied implications. *Mol. Plant* **15**, 104–124 (2022).
48. Yang, S. Y., Lin, W. Y., Hsiao, Y. M. & Chiou, T. J. Milestones in understanding transport, sensing, and signaling of the plant nutrient phosphorus. *Plant Cell* **36**, 1504–1523 (2024).
49. Rubio, V. et al. A conserved MYB transcription factor involved in phosphate starvation signaling both in vascular plants and in unicellular algae. *Genes Dev.* **15**, 2122–2133 (2001).
50. Zhou, J. et al. OsPHR2 is involved in phosphate-starvation signaling and excessive phosphate accumulation in shoots of plants. *Plant Physiol.* **146**, 1673–1686 (2008).
51. Guo, M. et al. Integrative comparison of the role of the PHOSPHATE RESPONSE1 subfamily in phosphate signaling and homeostasis in rice. *Plant Physiol.* **168**, 1762–1776 (2015).
52. Wang, Z., Zheng, Z., Zhu, Y., Kong, S. & Liu, D. PHOSPHATE RESPONSE 1 family members act distinctly to regulate transcriptional responses to phosphate starvation. *Plant Physiol.* **191**, 1324–1343 (2023).
53. Bustos, R. et al. A central regulatory system largely controls transcriptional activation and repression responses to phosphate starvation in Arabidopsis. *PLoS Genet.* **6**, e1001102 (2010).
54. Barragán-Rosillo, A. C. et al. Genome accessibility dynamics in response to phosphate limitation is controlled by the PHR1 family of transcription factors in Arabidopsis. *Proc. Natl. Acad. Sci. USA* **118**, e2107558118 (2021).
55. Pant, B. D. et al. The transcription factor PHR1 regulates lipid remodeling and triacylglycerol accumulation in Arabidopsis thaliana during phosphorus starvation. *J. Exp. Bot.* **66**, 1907–1918 (2015).
56. Pant, B. D. et al. Identification of primary and secondary metabolites with phosphorus status-dependent abundance in Arabidopsis, and of the transcription factor PHR1 as a major regulator of metabolic changes during phosphorus limitation. *Plant Cell Environ.* **38**, 172–187 (2015).
57. Shi, J. et al. A phosphate starvation response-centered network regulates mycorrhizal symbiosis. *Cell* **184**, 5527–5540.e5518 (2021).
58. Puga, M. I. et al. SPX1 is a phosphate-dependent inhibitor of Phosphate Starvation Response 1 in Arabidopsis. *Proc. Natl. Acad. Sci. USA* **111**, 14947–14952 (2014).
59. Wang, Z. Y. et al. Rice SPX1 and SPX2 inhibit phosphate starvation responses through interacting with PHR2 in a phosphate-dependent manner. *Proc. Natl. Acad. Sci. USA* **111**, 14953–14958 (2014).
60. Lv, Q. et al. SPX4 negatively regulates phosphate signaling and homeostasis through its interaction with PHR2 in rice. *Plant Cell* **26**, 1586–1597 (2014).
61. Dong, J. et al. Inositol pyrophosphate InsP(8) acts as an intracellular phosphate signal in Arabidopsis. *Mol. Plant* **12**, 1463–1473 (2019).
62. Guo, M. et al. A reciprocal inhibitory module for Pi and iron signaling. *Mol. Plant* **15**, 138–150 (2022).

63. Miura, K. et al. The Arabidopsis SUMO E3 ligase SIZ1 controls phosphate deficiency responses. *Proc. Natl. Acad. Sci. USA* **102**, 7760–7765 (2005).
64. Zhang, G. et al. Brassinosteroid-dependent phosphorylation of PHOSPHATE STARVATION RESPONSE2 reduces its DNA-binding ability in rice. *Plant Cell* **36**, 2253–2271 (2024).
65. Duan, K. et al. Characterization of a sub-family of Arabidopsis genes with the SPX domain reveals their diverse functions in plant tolerance to phosphorus starvation. *Plant J.* **54**, 965–975 (2008).
66. González, E., Solano, R., Rubio, V., Leyva, A. & Paz-Ares, J. PHOSPHATE TRANSPORTER TRAFFIC FACILITATOR1 is a plant-specific SEC12-related protein that enables the endoplasmic reticulum exit of a high-affinity phosphate transporter in Arabidopsis. *Plant Cell* **17**, 3500–3512 (2005).
67. Bayle, V. et al. Arabidopsis thaliana high-affinity phosphate transporters exhibit multiple levels of posttranslational regulation. *Plant Cell* **23**, 1523–1535 (2011).
68. Hamburger, D., Rezzonico, E., MacDonald-Comber Petétot, J., Somerville, C. & Poirier, Y. Identification and characterization of the Arabidopsis PHO1 gene involved in phosphate loading to the xylem. *Plant Cell* **14**, 889–902 (2002).
69. Svistoonoff, S. et al. Root tip contact with low-phosphate media reprograms plant root architecture. *Nat. Genet.* **39**, 792–796 (2007).
70. Zhu, J. et al. Two bifunctional inositol pyrophosphate kinases/phosphatases control plant phosphate homeostasis. *Elife* **8**, e43582 (2019).
71. Liu, J. et al. A vacuolar phosphate transporter essential for phosphate homeostasis in Arabidopsis. *Proc. Natl. Acad. Sci. USA* **112**, E6571–E6578 (2015).
72. Liu, T. Y. et al. Identification of plant vacuolar transporters mediating phosphate storage. *Nat. Commun.* **7**, 11095 (2016).
73. Castrillo, G. et al. Root microbiota drive direct integration of phosphate stress and immunity. *Nature* **543**, 513–518 (2017).
74. Zhong, S. X. et al. SERRATE drives phase separation behaviours to regulate m6A modification and miRNA biogenesis. *Nat. Cell Biol.* **26**, 2129–2143 (2024).
75. Bai, H. Y. et al. The METHYLTRANSFERASE B-SERRATE interaction mediates the reciprocal regulation of microRNA biogenesis and RNA m6A modification. *J. Integr. Plant Biol.* **66**, 2613–2631 (2024).
76. Wang, X. et al. A photoregulatory mechanism of the circadian clock in Arabidopsis. *Nat. Plants* **7**, 1397–1408 (2021).
77. Jiang, B. C. et al. Light-induced LLPS of the CRY2/SPA1/FIO1 complex regulating mRNA methylation and chlorophyll homeostasis in Arabidopsis. *Nat. Plants* **9**, 2042–2058 (2023).
78. Yankova, E. et al. Small-molecule inhibition of METTL3 as a strategy against myeloid leukaemia. *Nature* **593**, 597–601 (2021).
79. Sorenson, R. S., Deshotel, M. J., Johnson, K., Adler, F. R. & Sieburth, L. E. Arabidopsis mRNA decay landscape arises from specialized RNA decay substrates, decapping-mediated feedback, and redundancy. *Proc. Natl. Acad. Sci. USA* **115**, E1485–e1494 (2018).
80. Lin, S. I. et al. Regulatory network of microRNA399 and PHO2 by systemic signaling. *Plant Physiol.* **147**, 732–746 (2008).
81. Pant, B. D., Buhtz, A., Kehr, J. & Scheible, W. R. MicroRNA399 is a long-distance signal for the regulation of plant phosphate homeostasis. *Plant J.* **53**, 731–738 (2008).
82. Song, P. Z. et al. Arabidopsis N6-methyladenosine reader CPSF30-L recognizes FUE signals to control polyadenylation site choice in liquid-like nuclear bodies. *Mol. Plant* **14**, 571–587 (2021).
83. Yoon, Y., Soles, L. V. & Shi, Y. S. PAS-seq 2: a fast and sensitive method for global profiling of polyadenylated RNAs. *mRNA 3′ End. Process. Metab.* **655**, 25–35 (2021).
84. Hou, Y. F. et al. CPSF30-L-mediated recognition of mRNA m6A modification controls alternative polyadenylation of nitrate signaling-related gene transcripts in Arabidopsis. *Mol. Plant* **14**, 688–699 (2021).
85. Xiao, Y. et al. An elongation- and ligation-based qPCR amplification method for the radiolabeling-free detection of locus-specific N6-methyladenosine modification. *Angew. Chem. Int. Ed.* **57**, 15995–16000 (2018).
86. Huang, H. et al. Histone H3 trimethylation at lysine 36 guides m(6)A RNA modification co-transcriptionally. *Nature* **567**, 414–419 (2019).
87. Shim, S., Lee, H. G., Lee, H. & Seo, P. J. H3K36me2 is highly correlated with m(6) A modifications in plants. *J. Integr. Plant Biol.* **62**, 1455–1460 (2020).
88. Shao, Y., Wong, C. E., Shen, L. & Yu, H. N(6)-methyladenosine modification underlies messenger RNA metabolism and plant development. *Curr. Opin. Plant Biol.* **63**, 102047 (2021).
89. Parker M. T. et al. Nanopore direct RNA sequencing maps the complexity of Arabidopsis mRNA processing and m(6)A modification. *eLife.* **9**, e49658 (2020).
90. Wang, X. et al. N6-methyladenosine-dependent regulation of messenger RNA stability. *Nature* **505**, 117–120 (2014).
91. Du, H. et al. YTHDF2 destabilizes m(6)A-containing RNA through direct recruitment of the CCR4-NOT deadenylase complex. *Nat. Commun.* **7**, 12626 (2016).
92. Huang, H. et al. Recognition of RNA N(6)-methyladenosine by IGF2BP proteins enhances mRNA stability and translation. *Nat. Cell Biol.* **20**, 285–295 (2018).
93. Wei, L. H. et al. The m6A reader ECT2 controls trichome morphology by affecting mRNA stability in arabidopsis. *Plant Cell* **30**, 968–985 (2018).
94. Reis, R., Deforges, J., Clua, J. & Poirier Y. Alternative promoter usage modulates miRNA-guided translation inhibition of a m6A reader in phosphate starvation. Preprint at *bioRxiv*. (2020).
95. Reis, R. S. et al. Phosphate deficiency alters transcript isoforms via alternative transcription start sites. *Plant J.* **120**, 218–233 (2024).
96. Zhang, X., Henriques, R., Lin, S. S., Niu, Q. W. & Chua, N. H. Agrobacterium-mediated transformation of Arabidopsis thaliana using the floral dip method. *Nat. Protoc.* **1**, 641–646 (2006).
97. Carbonell, A. et al. Highly specific gene silencing in a monocot species by artificial microRNAs derived from chimeric miRNA precursors. *Plant J.* **82**, 1061–1075 (2015).
98. Yu, Q. et al. RNA demethylation increases the yield and biomass of rice and potato plants in field trials. *Nat. Biotechnol.* **39**, 1581–1588 (2021).
99. Martin, M. Cutadapt removes adapter sequences from high-throughput sequencing reads. *EMBnet. J.* **17**, 10–12 (2011).
100. Kim, D., Paggi, J. M., Park, C., Bennett, C. & Salzberg, S. L. Graph-based genome alignment and genotyping with HISAT2 and HISAT-genotype. *Nat. Biotechnol.* **37**, 907–915 (2019).
101. Thorvaldsdóttir, H., Robinson, J. T. & Mesirov, J. P. Integrative Genomics Viewer (IGV): high-performance genomics data visualization and exploration. *Brief. Bioinform.* **14**, 178–192 (2013).
102. Quinlan, A. R. & Hall, I. M. BEDTools: a flexible suite of utilities for comparing genomic features. *Bioinformatics* **26**, 841–842 (2010).
103. Liao, Y., Smyth, G. K. & Shi, W. featureCounts: an efficient general purpose program for assigning sequence reads to genomic features. *Bioinformatics* **30**, 923–930 (2014).
104. Love, M. I., Huber, W. & Anders, S. Moderated estimation of fold change and dispersion for RNA-seq data with DESeq2. *Genome Biol.* **15**, 550 (2014).
105. Wang, Z. Y. et al. SWI2/SNF2 ATPase CHR2 remodels pri-miRNAs via Serrate to impede miRNA production. *Nature* **557**, 516–521 (2018).
106. Chen, C. et al. TBtools: an integrative toolkit developed for interactive analyses of big biological data. *Mol. Plant* **13**, 1194–1202 (2020).
107. Gu, Z., Eils, R. & Schlesner, M. Complex heatmaps reveal patterns and correlations in multidimensional genomic data. *Bioinformatics* **32**, 2847–2849 (2016).

Acknowledgements
We thank Hang Su (Institute of Botany, Chinese Academy of Sciences) for the assistance with the LC-MS/MS assay. We thank Wei Yin (the Core Facilities, Zhejiang University School of Medicine) for the technical support for fluorescent imaging. This work was supported by grants from the Natural Science Foundation of Zhejiang Province, China (LR24C150001 and LZ22C150002), the National Natural Science Foundation of China (32170262), the National Key Research and Development Program of China (2021YFF1000402 and 2022YFD1401600) and the Fundamental Research Funds for the Central University (226202400102) to Z.W., the National Natural Science Foundation of China (32170593) and the Guangdong Provincial Pearl River Talent Plan (2019QN01N108) to Z.Z.

Author contributions
Z.W. conceived the project and designed the experiments; K.L., X.W., J.W., S.W., H.B., L.Q. performed the experiments; K.L. conducted the data analyses, with assistance from W.D. and Q.J.; G-Z.L., and Z.Z. provided intellectual support. Z.W. and K.L. wrote the manuscript with input from all authors.

Competing interests
The authors declare no competing interests.

Additional information
Supplementary information The online version contains supplementary material available at https://doi.org/10.1038/s41467-025-59331-y.

Correspondence and requests for materials should be addressed to Zhiye Wang.

Peer review information *Nature Communications* thanks Guifang Jia and the other, anonymous, reviewers for their contribution to the peer review of this work. A peer review file is available.

Kai Liu[1], Xiaojia Wang[1], Jingyi Wang[1], Shuman Wang[1], Haiyan Bai[2], Weiguo Dong[1], Lulu Qiao[1], Qiongli Jin[1], Zhonghui Zhang[2], Guan-Zheng Luo[3] & Zhiye Wang[1,4] ✉

[1]State Key Laboratory of Plant Environmental Resilience, College of Life Sciences, Zhejiang University, Hangzhou, Zhejiang, China. [2]Guangdong Provincial Key Laboratory of Biotechnology for Plant Development, School of Life Science, South China Normal University, Guangzhou, China. [3]MOE Key Laboratory of Gene Function and Regulation, Guangdong Province Key Laboratory of Pharmaceutical Functional Genes, State Key Laboratory of Biocontrol, School of Life Sciences, Sun Yat-sen University, Guangzhou, China. [4]The First Affiliated Hospital, College of Medicine, Zhejiang University, Hangzhou, Zhejiang, China. ✉e-mail: wangzhiye1@zju.edu.cn